Summary of the 6th Propulsion Aerodynamics Workshop: NASA 1507 Inlet

Miguel Moreno[1], Pavlos K. Zachos[2]
School of Aerospace, Transport and Manufacturing, Cranfield University, UK

Erick J. S. Gantt[3]
Cadence Design Systems, Inc., San Jose, CA, US

Luiz Tobaldini Neto[4], Diego Ferolla de Abreu[5]
Embraer SA, Sao Jose dos Campos, São Paulo, Brazil

Neal D. Domel[6]
Lockheed Martin Aeronautics Company, Fort Worth, Texas, USA

John W. Slater[7]
NASA John H. Glenn Research Center, Cleveland, Ohio, USA

The 6th AIAA Propulsion Aerodynamics Workshop (PAW6) was held as part of AIAA's Science and Technology Forum between January 21st -22nd 2023 in National Harbor, US. The goal of the workshop was to evaluate the current capability of computational fluid dynamics (CFD) on complex flows, pertinent to the high-speed propulsion community. PAW6 inlet test case was a mixed-compression supersonic inlet referred to here as the NASA 1507 inlet which featured a complex shock system attached at the entry along with a range of different flow control methods such as porous bleeds and vortex generators. Among several experimental test cases, four were selected for the workshop across a range of back-pressures, or inlet flow ratios, that yield different levels of pressure recovery, engine face distortion and bleed flows. Flow prediction data from 8 different participants was submitted using a total of 5 different computational domains for which 9 computational grids were developed and provided by Cadence. In general, flow predictions were better able to match the test data near the critical point of intake operation regardless of the flow solver, grid refinement level or turbulence model. Models with fully resolved rather than modelled bleed and/or vortex generators showed better results. Across the sub-critical range of operation, a notable under prediction of the flow ratio was seen across all flow solvers and models, indicating significant variations in the porous bleed modelling between the CFD datasets. The work indicates that more effort is needed by the relevant community toward the development of robust predictive capabilities, especially when complex flow control systems are in place for stability across the operating range.

[1] Doctoral Researcher, Centre for Propulsion and Thermal Power Engineering, Cranfield University.
[2] Reader in Propulsion Aerodynamics, Centre for Propulsion and Thermal Power Engineering. AIAA Member.
[3] Sr. Principal Application Engineer, Worldwide Field Operations. AIAA Senior Member.
[4] Propulsion Systems Engineer, Chief Engineer Office.
[5] Propulsion Systems Engineer, Chief Engineer Office.
[6] Aeronautical Engineer Senior Staff, Propulsion Integration and CFD. AIAA Associate Fellow.
[7] Research Aerospace Engineer, Inlets and Nozzles Branch, Propulsion Division. AIAA Associate Fellow.

Nomenclature

A	*Inlet model A*
B	*Inlet model B*
C	*Inlet model C*
D	*Inlet model D*
E	*Inlet model E*
BL	*Boundary Layer*
CFD	*Computational Fluid Dynamics*
CB	*Centerbody*
CI	*Cowl Interior*
EF	*Engine Face*
SG	*Structured Grid*
MIME	*Multipurpose Intelligent Meshing Environment (METACOMP)*
2D	*Two-Dimensional*
3D	*Three-Dimensional*
KKL	*K-KL turbulence model*
LM	*Langtry-Menter turbulence model*
SA	*Spalart-Almaras turbulence model*
SST	*Shear Stress Transport turbulence model*
h	*Boundary layer height (inches)*
$\dot{m}$	*Mass flow (kg/s)*
p	*Static pressure (Pa)*
P	*Total pressure (Pa)*
R_c	*Centerbody radius (inches)*
t	*Static temperature (K)*
T	*Total temperature (K)*
p^*	*Adjusted plenum pressure*
t^-	*Reduced plenum throat*
x^*	*Modified axial positions for measurements*

Subscripts

2	*Bleed surface property*
∞	*Freestream property*

I. Test Case Description

The simulation of a mixed-compression intake is complex as it would have to account for intake stability, complex shock systems, integration of porous bleed areas including control plenums with different operating curves and the presence of vortex generators and their downstream field influence. To the present time, no PAW workshop featured a similar case, and to the authors' best knowledge, no other study validated the performance of an air breathing engine accounting for all those subsystems. Standalone mixed-compression inlet configurations [1] [2] or inlets with vortex generators [3] have been previously shown in the literature, yet the complexity or nature of those cases is different to the one found in a mixed-compression inlet operating at high speeds.

The NASA 1507 inlet, fully described previously by Sorensen and Smeltzer in [4], is an axisymmetric spike mixed-compression inlet designed to cruise at Mach 3. A very similar inlet can be seen on the Lockheed SR-71 Blackbird aircraft and its precursor the A-12 (Figure 1). Key aspects of this inlet configuration are the use of multiple porous bleed zones to establish a stable internal shock system and the use of a vortex generator array between the bleed regions and the engine face to manage the flow distortions in certain parts of the operating envelope (Figure 2). The centerbody and cowl interior were axisymmetric with respect to the axis of the inlet, which coincided with the axis of the engine-face. The planar profiles of the centerbody and cowl interior were presented in the report by a set of axial and radial coordinates extending from their start to the engine face. The centerbody started at the tip or nose of the conical external supersonic diffuser which had a half-angle of approximately 12.5 degrees. The cowl interior started at the cowl lip with an interior angle of zero degrees to reduce the cowl exterior wave drag. The length of the inlet was approximately 4.6 feet. An overall planar view of the inlet that was installed and tested at NASA Ames is shown in Figure 3.

The forward portion of the cowl translated axially to adjust the cross-sectional area through the inlet's interior duct. This ability to translate allowed the inlet to start by varying the position and size of the throat area, which established the internal supersonic compression with oblique shock waves and a terminal normal shock. The inlet design placed the cowl lip at $(x/Rc)lip = 2.375$. However, the cowl coordinates for test case of interest for the PAW had the cowl translated so that $(x/Rc)lip = 2.330$.
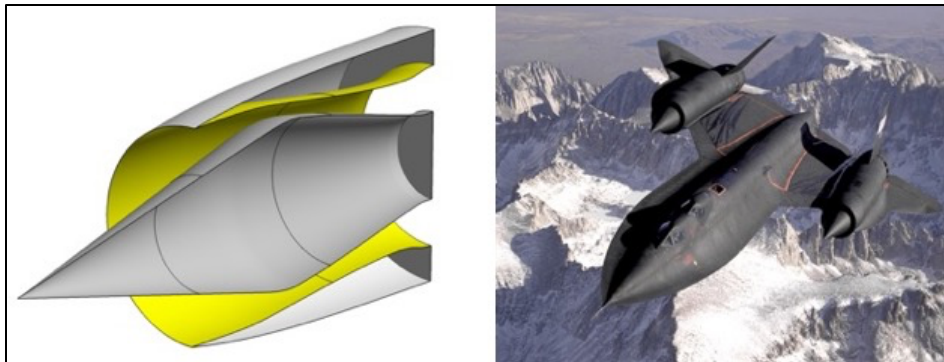

Figure 1 The NASA 1507 inlet as shown in the PAW6 inlet guide [5] (left) and a similar inlet installed on a Lockheed SR-71 Blackbird (right) [Image credits: USAF / Judson Brohmer, Public domain, via Wikimedia Commons].
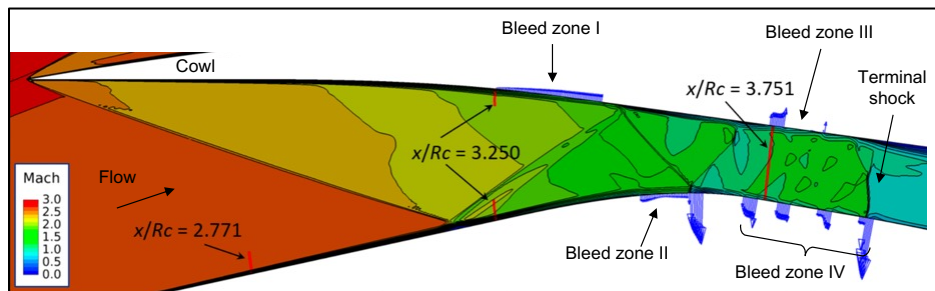

Figure 2 NASA 1507 internal shock system, location of bleed zones and rake measurement stations [5].
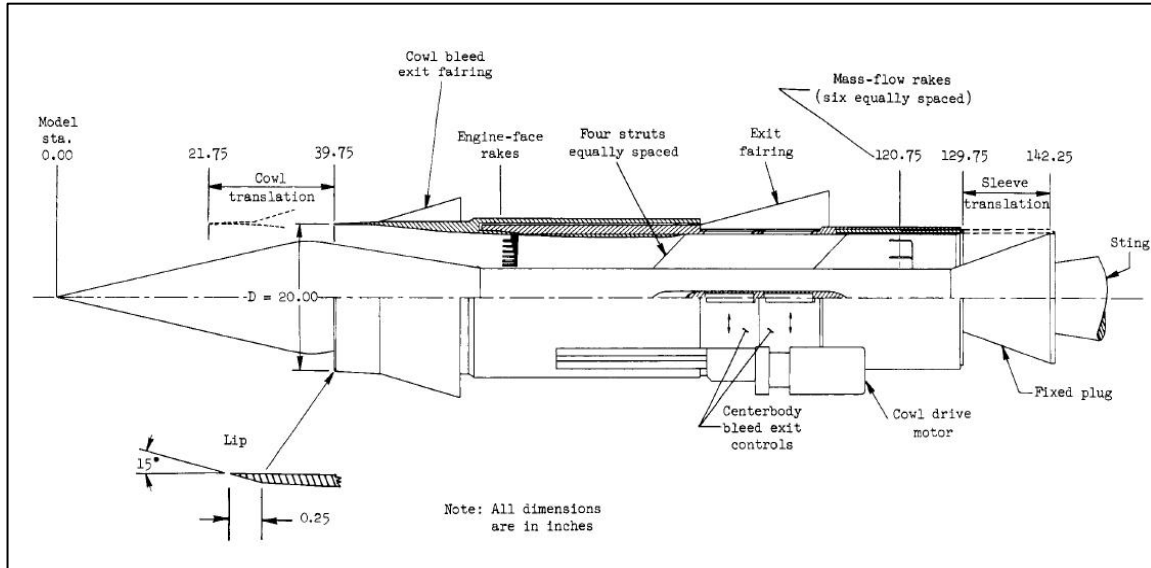
Figure 3 Symmetry plane view of the NASA 1507 inlet wind-tunnel installation [4].

The stability of the shock system required four porous bleed zones through the inlet. The bleed zones and related information are shown in Figure 2 and Figure 4 which is reproduced from [4]. Bleed zones I and II were placed upstream of the shockwave impingements to limit the boundary layer growth. Bleed zone I was located on the cowl between $x/Rc = 3.3$ and 3.5. Bleed zone II was located on the centerbody between $x/Rc = 3.456$ and 3.644. These bleed zones were considered performance bleed zones intended to improve the boundary layer approaching the geometric throat. Bleed zones III and IV were placed at the throat section to control the stability of the terminal shock and prevent unstarting. Bleed zone III comprises two bleed rows at $x/Rc = 3.846$ and 3.928, and zone IV four bleed rows at $x/Rc = 3.751, 3.816, 3.897$ and 3.979. Each bleed zone had separate plenum and ducting to avoid recirculation from a bleed zone of higher pressure (downstream zones) to one of lower pressure (upstream zones). Each bleed zone had its own controllable exits whereby the bleed flow rate could be adjusted. The bleed exits were fitted with fairings to ensure a low-pressure exit for the bleed flow. For the inlet configuration of interest in this PAW test case, the bleed configuration is referred to as bleed B [5].

The inlet featured vortex generators about the circumference of the centerbody and cowl interior downstream of the throat section at $(x/Rc) = 4.1$. The purpose of the vortex generators was to mix some of the core inlet flow with the boundary layer flow to limit regions of low momentum within the inlet flow through the subsonic diffuser as it approached the engine face. Such mixing has the potential of reducing total pressure distortion, which can be damaging to a turbine engine. The engine-face station was located at $x/Rc = 5.5$. An engine-face rake was located at this axial station to assess the total pressure radial profiles along the annular cross-section (Figure 4). All engine-face experimental results presented herein are based on the radial profiles provided by Rake 1 (Figure 5)

Downstream of the engine face, the internal ducting was a constant-area annular duct with a length of 6.2 feet. Four support struts equally spaced about the circumference connected the cowl to the centerbody. The centerbody of the annular duct ended with a fixed plug, which as attached to a tunnel support sting. The position of the terminal shock was adjusted in the wind-tunnel tests by the translation of a sleeve within the cowling. With a change in position, the minimum cross-sectional area of the flow passage through the plug varied. The flow was choked at the minimum cross-section area, and so, when the cross-section area was made smaller, the backpressure increased.

The wind-tunnel test of the NASA 1507 inlet includes boundary-layer profiles consisting of total pressure measurements through the boundary layers for three rakes on the centerbody and two rakes on the cowl interior (Figure 2). The first centerbody rake at x/Rc = 2.771 (x = 2.309 ft) is ahead of the impingement point on the centerbody for the cowl shock, and so, provides a good measure of the boundary layer on the centerbody entering the inlet. The full profile of the boundary layer suggests that the forward portion of the external supersonic diffuser had laminar flow. The boundary layer profile data provides a means of estimating the extent of laminar flow by adjusting computational flow modelling to match the boundary-layer profile. The second centerbody rake at x/Rc = 3.250 (x = 2.708 ft) is just downstream of the impingement point for the cowl shock, and so, provides a means of assessing the effects of the impingement on the boundary layer as it approaches bleed region II and the geometry throat. The first cowl rake at

x/Rc = 3.250 (x = 2.708 ft) is ahead of bleed zone I and the impingement point for the reflected shock from the centerbody. The data of this rake provides a measure of the state of the boundary layer on the cowl interior as it approaches the bleed region and the geometric throat. The centerbody and cowl rake at x/Rc = 3.751 (x = 3.126 ft) assess the state of the boundary layers as they approach bleed zones III and IV.
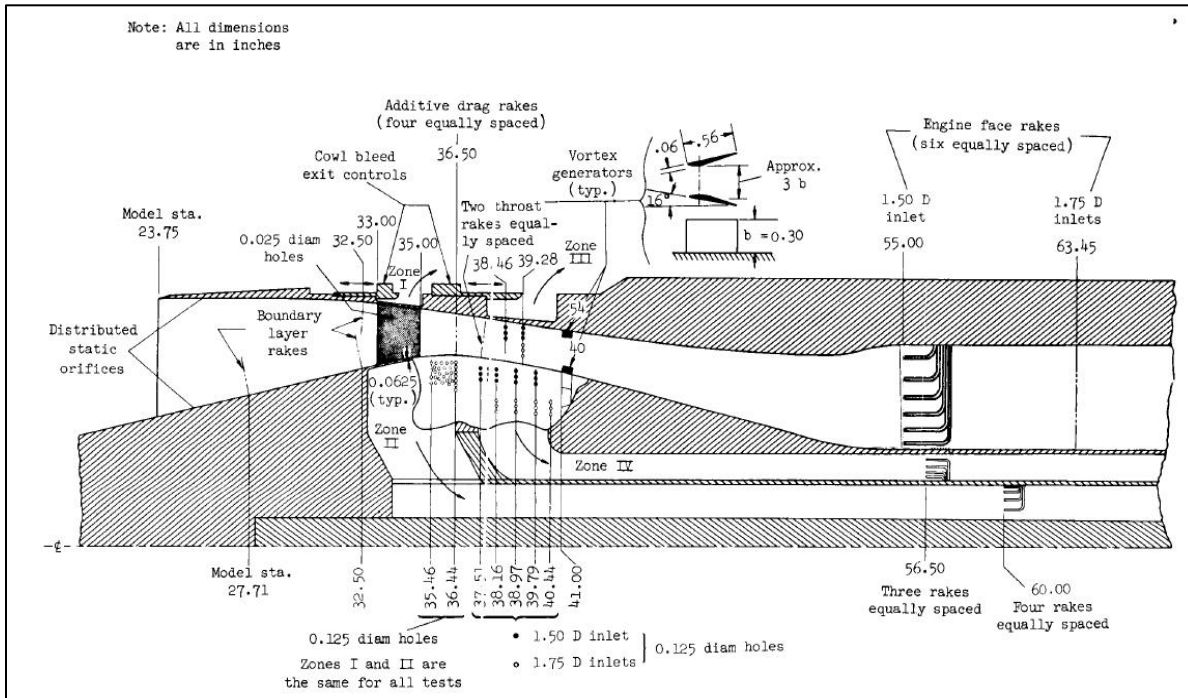

Figure 4 Features of the bleed regions and vortex generators along with coordinates through the internal ducting of the NASA 1507 inlet [4].
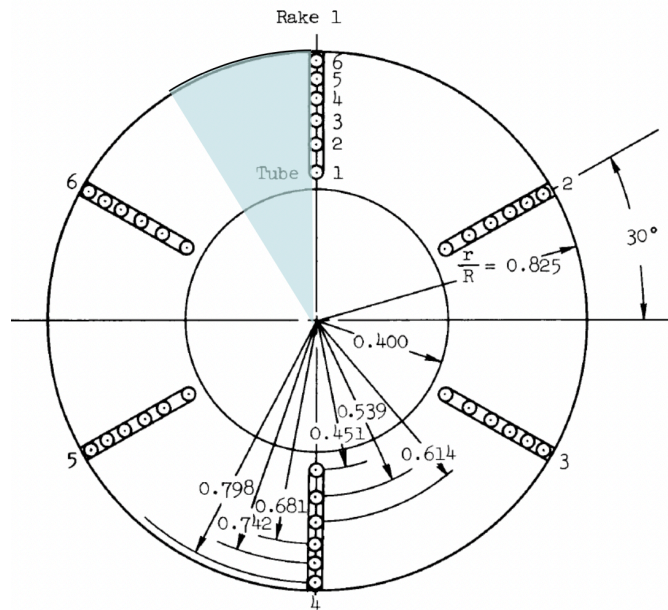

Figure 5 Engine-face station indicating distortion rake locations [4] (27-degree modelled sector shaded in blue).

Among the several cases, three (3) were selected for the workshop across a range of back-pressures, or inlet flow ratios, that yield different levels of pressure recovery, engine face distortion and bleed flows. In addition to the inlet performance data, the wind-tunnel available datasets included boundary layer characteristics, static pressure distributions along the centerbody and the cowl, and engine face total pressure rake data. The selected test cases are fully described in the PAW6 Inlet Guide that was distributed to the participants prior to the workshop and can be found in [5]. In summary, one mandatory case was included (Case 2) along with two optional test cases (Cases 4, 5 and 8) as shown in Figure 6. Wind tunnel freestream reference conditions as well as porous bleed flow rates are also indicated in Figure 6.

INFO TABLE 1 - Wind-Tunnel Test Section Conditions for Mach 3 Test Cases

These conditions correspond to the inlet configuration at zero angle-of-attack, 1.5D subsonic diffuser with vortex generators, cowl lip position at $(x/R_C) = 2.33$, and bleed exit setting B.

M_∞	3.00		γ	1.4				Inlet Reference Capture Properties			
$p_{t\infty}$	15.0	psi	R	1716.235	ft lbf / slug R		R_C	10.0	in	0.8333	ft
p_∞	0.4084	psi	g_c	32.174	lbm/slug		D_C	20.0	in	1.6667	ft
Rn	2.00E+06	/ft					A_C	314.16	in^2	2.1817	ft^2
T_∞	220.0	^{o}R					m_∞	0.7411	slug/sec	23.844	lbm/s
$T_{t\infty}$	616.0	^{o}R									

INFO TABLE 2 - Supercritical bleed rates and plenum pressures for test case 2					
Bleed	m_{bl}/m_∞	m_{bl}	m_{bl}	p_{tbl}	$p_{tbl}/p_{t\infty}$
	(%)	(slug/s)	(lbm/s)	(psi)	
I	2.11%	0.0156	0.5025	1.790	0.119
II	1.82%	0.0135	0.4328	2.247	0.150
III	0.80%	0.0059	0.1901	1.568	0.105
IV	2.40%	0.0178	0.5732	2.822	0.188
Total	7.12%	0.0528	1.6987		

m_2/m_∞	Engine-face flow ratio
$p_{t2}/p_{t\infty}$	Inlet total pressure recovery
m_{bl}/m_∞	Total inlet bleed ratio from all four bleed zones
$m_{bl\#}/m_\infty$	Bleed ratio from bleed zone #
m^*_{bl}/m_∞	Sum of bleed ratios from each bleed zone
m^*_{blpl}/m_∞	Bleed ratio from bleed plenum pressure plots
$p_{tbl1}/p_{t\infty}$	Bleed plenum pressure ratio

INFO TABLE 3 - Characteristic Curve Data for Mach 3.0 1.50D Inlet. Vgs. (x/R)lip = 2.330. Bleed exit setting B													
Test Case	m_2/m_∞	$p_{t2}/p_{t\infty}$	Δp_{t2}	m_{bl}/m_∞	m_{bl1}/m_∞	m_{bl2}/m_∞	m_{bl3}/m_∞	m_{bl4}/m_∞	m^*_{bl}/m_∞	$p_{tbl1}/p_{t\infty}$	$p_{tbl2}/p_{t\infty}$	$p_{tbl3}/p_{t\infty}$	$p_{tbl4}/p_{t\infty}$	m^*_{blpl}/m_∞
2	0.946	0.814	0.108	0.071	0.0211	0.0182	0.0080	0.0240	0.071	0.119	0.150	0.105	0.188	0.071
4	0.919	0.885	0.087	0.086	0.0207	0.0178	0.0139	0.0326	0.085	0.122	0.152	0.190	0.264	0.086
5	0.907	0.894	0.077	0.096	0.0207	0.0176	0.0178	0.0386	0.095	0.122	0.153	0.240	0.305	0.096
8	0.883	0.910	0.062	0.109	0.0209	0.0176	0.0218	0.0477	0.108	0.124	0.159	0.302	0.388	0.109

Figure 6 Case setup parameters for Cases 2, 4 and 8 along with wind tunnel onset conditions as distributed to the PAW6 participants [5]. Nomenclature corresponding to the properties of this figure is included.

II. Computational Models and Grid Specifications

A four-level unstructured grid family composed of tetrahedra, prisms, pyramids, and hexahedra were generated by Cadence using Fidelity™ Pointwise® and provided to participants. The volume grids modelled the inlet flow physics in diverse ways, regarding the bleed system and vortex generators treatment. The bleed boundary condition used at the corresponding inlet surfaces were previously presented by Slater [6] [7] or used Bush and Frink models [8]. The vortex generator models relied on the introduction of sources via BAY models [9] with some in-house modifications for accuracy in the cases of some participants.

The geometrical models used for the flow simulations were as follows:

- **Model A**: all bleed regions I to IV in Figure 7 are modelled as surfaces with sources. Vortex generators are modelled as sources. Model A was used to produce a simplified two-dimensional axisymmetric grid, which allowed participation from users with limited computational resources, requiring the user to apply a lumped-element bleed boundary condition to each.
- **Model B**: all bleed regions I to IV in Figure 8 are modelled as surfaces with sources. No notion of vortex generators was included.
- **Model C**: all bleed regions I to IV in Figure 9 are modelled as surfaces with sources. Vortex generators are fully resolved and meshed as airfoil profiles.
- **Model D**: performance bleed zones I to II in Figure 10 are modelled as surfaces, and stability bleed zones III to IV are physically meshed in geometry with discrete holes and plenums. Vortex generators are fully resolved and meshed as airfoil profiles.
- **Model E**: performance bleed zones I to II in Figure 11 are modelled as surfaces, and stability bleed zones III to IV are physically meshed in geometry with discrete holes and plenums. Vortex generators are modelled as sources.

For each model a family of grids was provided that included three resolution levels: coarse, medium, and fine. Three 3D grid families, each with three resolution levels, resulted in a total of nine 3D grids. These nine grids were created as a courtesy by Cadence Design Systems with the Fidelity™ Pointwise® grid generation tool. Cell statistics for the mesh families can be found in Table 1.
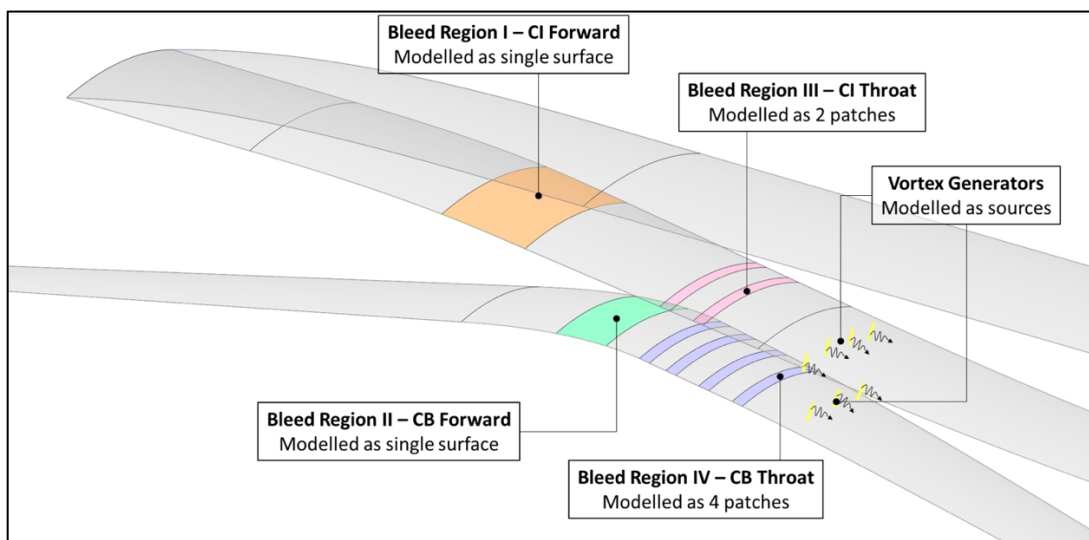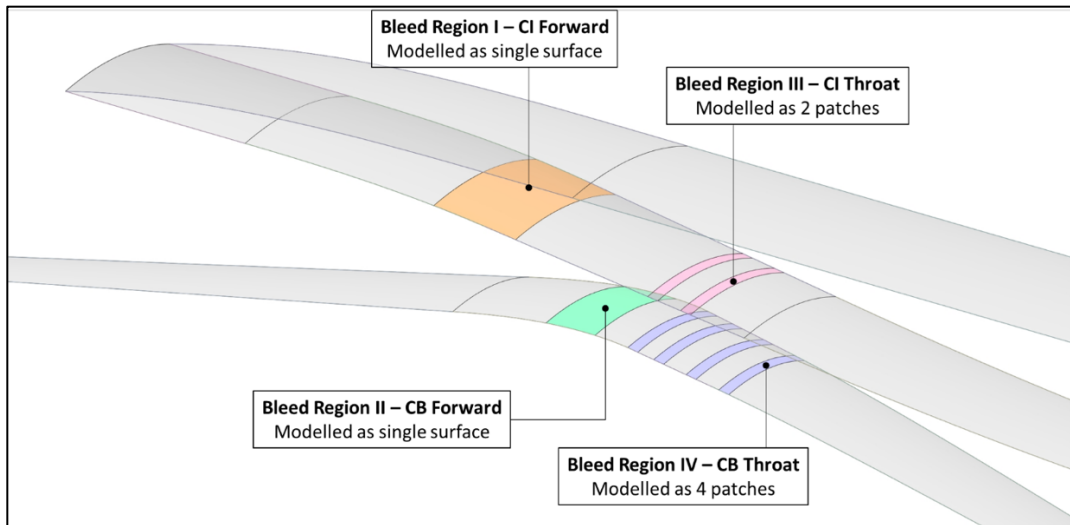

Figure 7 Definition of Model A.
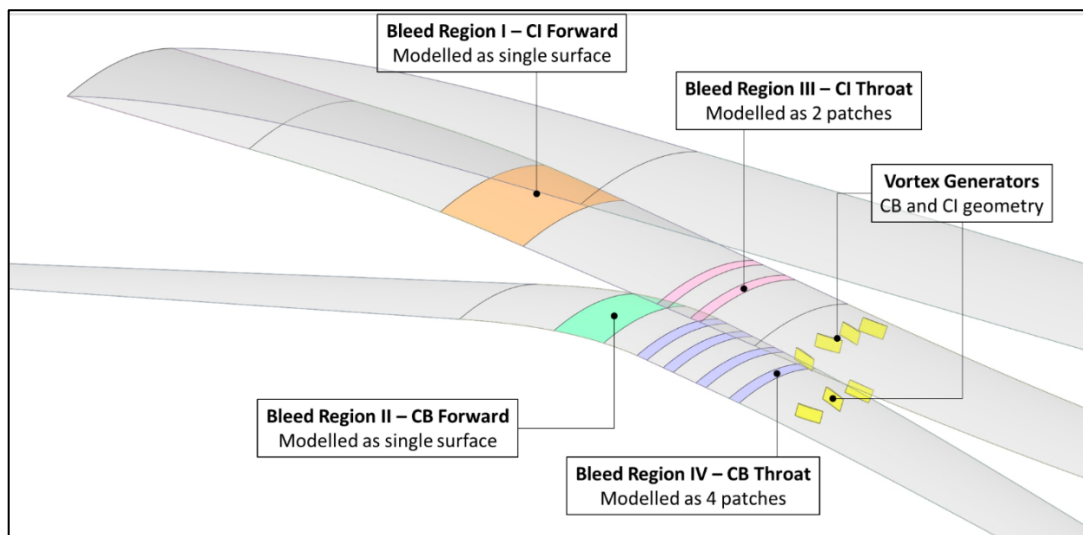
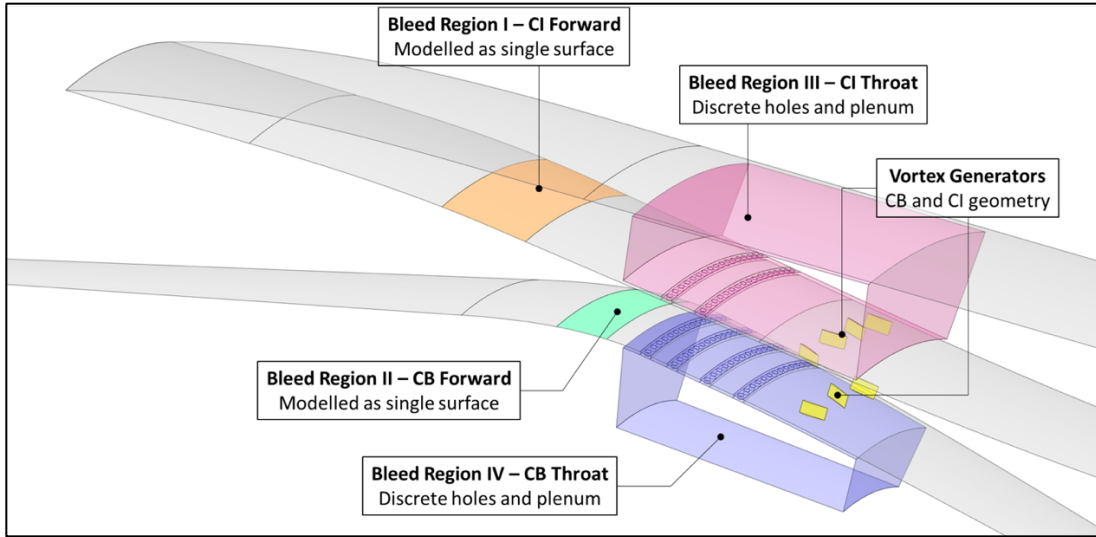**Figure 8 Definition of Model B.**

Figure 9 Definition of Model C.

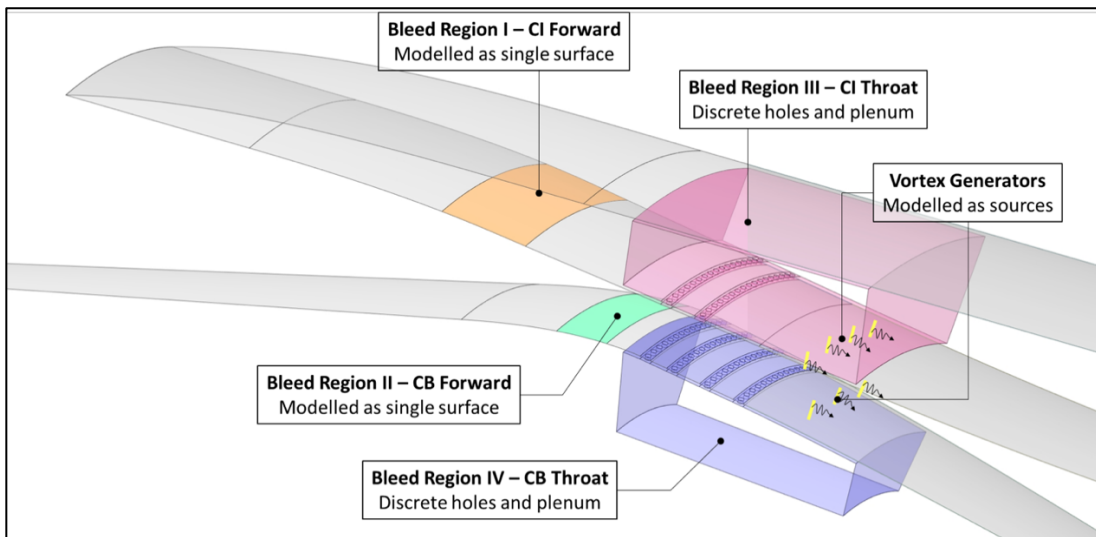**Figure 10 Definition of Model D.**

Figure 11 Definition of Model E.

Table 1 Cell and Point Statistics for the Workshop Provided 3D Meshes.

Model	Grid Level	Total Cells	Total Nodes	Hexahedra	Tetrahedra	Prisms	Pyramids
B	Coarse	9,760,473	3,888,632	0	3,226,568	6,462,351	71,554
B	Medium	23,747,837	9,444,086	0	7,842,651	15,760,090	145,096
B	Fine	78,208,705	27,227,527	0	37,184,170	40,689,253	335,282
C	Coarse	13,627,225	5,920,716	0	3,077,807	10,414,774	134,644
C	Medium	33,533,765	14,580,875	0	7,495,001	25,764,179	274,585
C	Fine	101,790,854	39,732,966	0	35,984,596	65,151,435	654,823
D	Coarse	22,960,643	10,152,442	0	4,585,751	18,162,542	212,350
D	Medium	73,440,545	32,303,329	0	15,068,066	57,848,353	524,126
D	Fine	203,789,205	84,947,307	0	55,504,448	147,016,344	1,268,413

Construction of the 3D grid families took advantage of the Automatic Surface Mesh tool in Fidelity™ Pointwise® to create the surface grids for the cowl and centerbody geometry components. This tool accepts global and local meshing goals or targets and generates a set of boundary matched surface grids where those goals include criteria such as surface curvature representation and cell aspect ratio limitation. These were joined by manually created symmetry style surface grids at the sides of the 27-degree wedge of the geometry both internal and external to the inlet. An external far boundary was created with extents to match that of the Model A 2D axisymmetric mesh. The coarse level Model D mesh was created first, being the most complex geometrically. Figure 12 shows a side view of the overall grid.
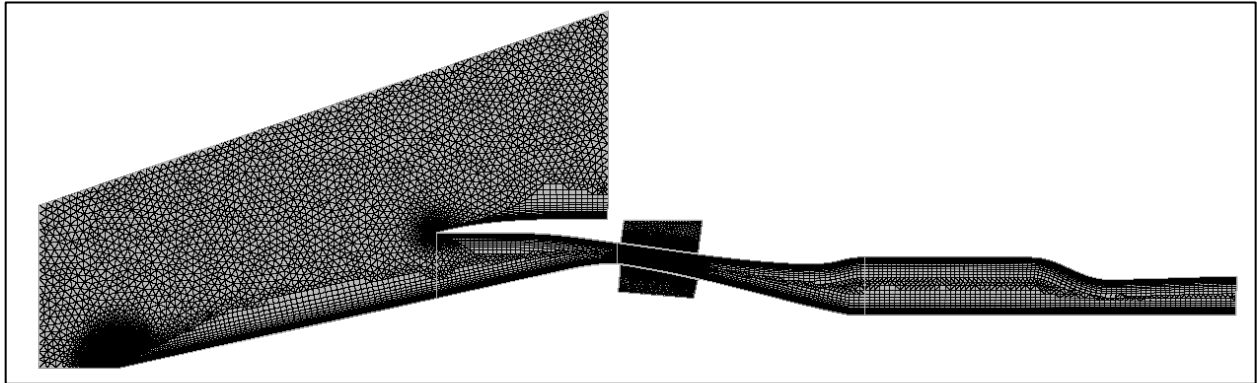
Figure 12 Profile view of Coarse Mesh Model D.

Coarse level grids for Models C and B were generated as successive modifications, respectively, to the coarse grid of Model D. This could easily be done by removing original surface grids representing unneeded geometry and replacing them with simple surface grids filling the original perimeter of those removed. For instance, the Model C level coarse grid no longer required the plenums and bleed holes to be represented. A single band of surface grid could then replace the original which included the holes, shown in Figure 13. Producing the less complex configurations in this way was not only an easier path in meshing, but it also has the benefit of producing the most similar meshes across the geometry variations given each retains the remaining original surface grid topology of the coarse Model D grid. Each coarse grid was then refined globally using a scripted refinement procedure to produce the medium and fine meshes, employing a refinement factor of 2.0 while targeting approximate total cell counts recommended by the workshop committee.
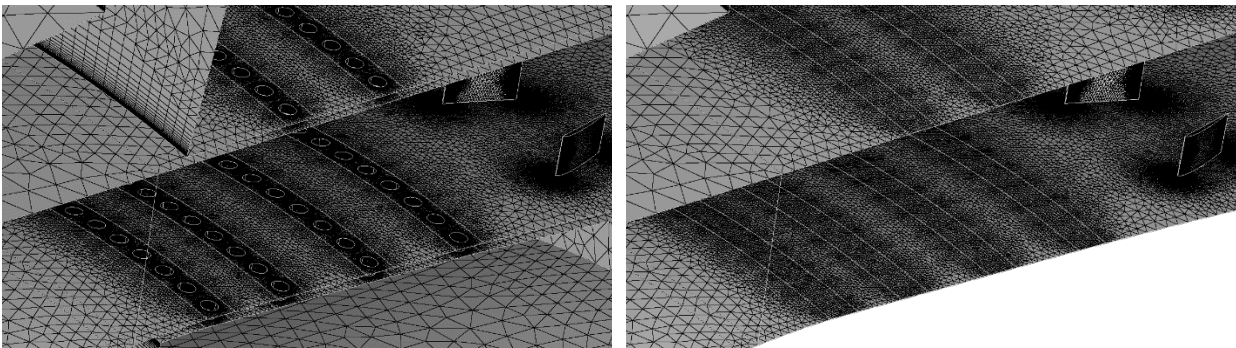

Figure 13 Geometry simplification from Mesh Model D (left) to Model C (right).

Wall adjacent boundary layer growth, shown in Figure 12, was produced using the Fidelity™ Pointwise® T-Rex anisotropic extrusion tool. As the surface grids are entirely triangulated for these grid families, the tool produces prism cells in the boundary layers, along with pyramids to cap exposed quad faces of prism cells, while the remaining volume was initialized with tetrahedra. Initial spacings, in inches, for the three refinement levels: coarse, medium, and fine are 1.0e-04, 5.0e-05, and 2.5e-05 respectively. All meshes used the same 20% growth in the boundary layers.

Additional refinement was introduced to the volume mesh in the Grid B meshes by incorporating the original vortex generator surface grids, in their original locations, as local refinement sources. Refinement was also added at the centerbody nose, shown in Figure 14, for all three geometry variations (Grids B, C and D), as early attempts to generate T-Rex layers fully to the nose produced fewer layers than desired. Therefore, local spacing in the surface grid and volume at the nose was refined to the wall spacing, producing fully isotropic mesh resolution at that spacing. An analytic sphere source was used to drive this refinement, with the target spacing relaxing in the radial direction away from the nose in all directions. The isotropic refinement transitions smoothly into the T-Rex layers as that method is designed to automatically end extrusion at isotropic cell heights. Target spacings for the spherical source were adjusted accordingly for each refinement level to match the wall spacing.
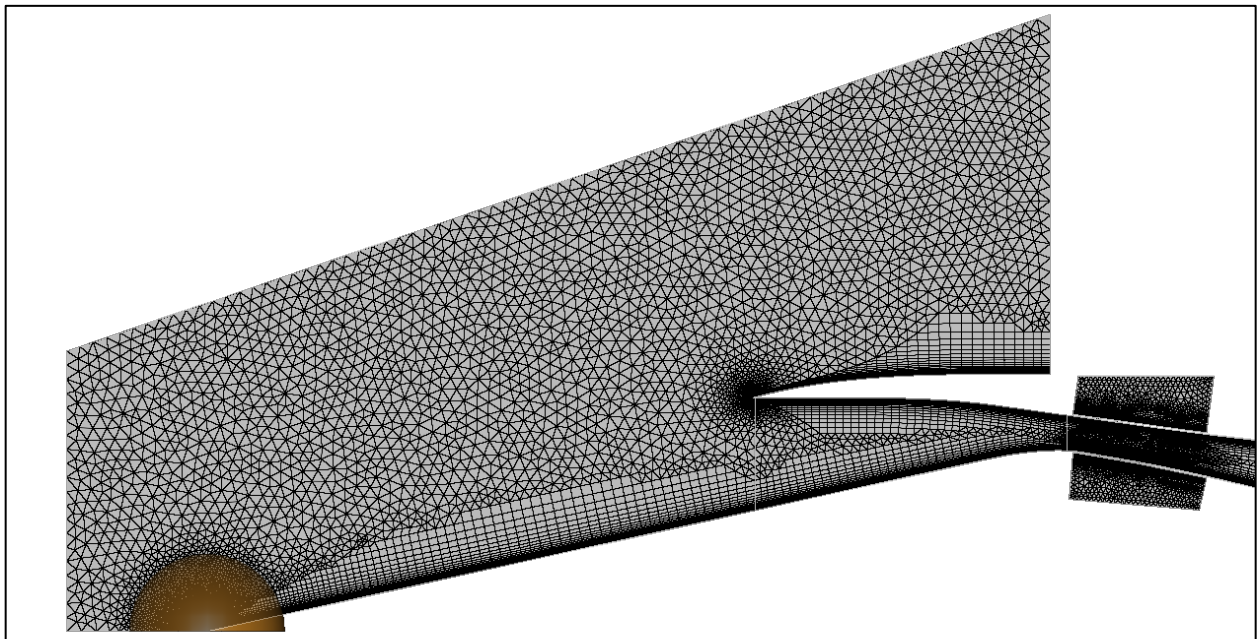

Figure 14 Profile closeup view of Coarse Mesh Model D showing source at centerbody nose.

For all mesh families the Bleed Regions I and II were modelled as boundary condition patches and therefore in the meshes each of these regions was provided as a separate surface grid and designated boundary condition at export for ease of assignment in participants' respective analysis software. Bleed Regions III and IV were modeled as geometric bleed holes in Model D and therefore these bleed holes are meshed through to the plenum geometries. Near wall layers generated throughout the duct were wrapped through these bleed holes and into the plenums. Only the surface containing the holes in the plenums received wall growth layers, while the remaining sides have force matching of the layers in the surface grids. The surface opposite the holes in the plenums are treated with fully isotropic surface meshes. For Models C and B, like Bleeds I and II for all models, the Bleeds III and IV are reduced to boundary condition patches. Therefore, for Models C and B, these bleeds have a single surface grid applied per each row and exported as a distinct boundary condition for later assignment.

Models D and C for this study provided geometric representation of the vortex generators as shown in Figure 10 and Figure 9, respectively. These features of the geometry were meshed along with the remaining centerbody and cowl using the Automatic Surface Mesh feature of Fidelity™ Pointwise®. Model B, shown in Figure 8, does not include the vortex generators. However, there was interest in maintaining local refinement in the Grid B meshes in the locations of the missing generators. Therefore, the root grid topology of the generators was preserved and converted

to surface grids with the shape of the root profile. Additionally, the original blade sides and tip surface grids used in Models D and C were retained to serve as volume refinement source entities for Model B grids. The topology of those surface grids, as sources, is not included directly as part of the volume interior of Model B, they only supply local refinement targets for the mesh generated.

All grid family meshes provided by Cadence were created and exported as four separate volume zones shown by color in Figure 15. Divisions were placed to facilitate boundary availability at key locations for later integration of flow properties at desired stations: cowl aperture, throat, and engine face. Additionally, for the Model D meshes, the exit from the cowl side plenum was split into four equal radial bands, as separate solver boundary conditions, so that study participants could more easily control exit conditions of the plenum and therefore the bleed rate for the cowl side bleed holes. This treatment was deemed unnecessary for the centerbody side plenum, so only a single exit boundary condition is applied.
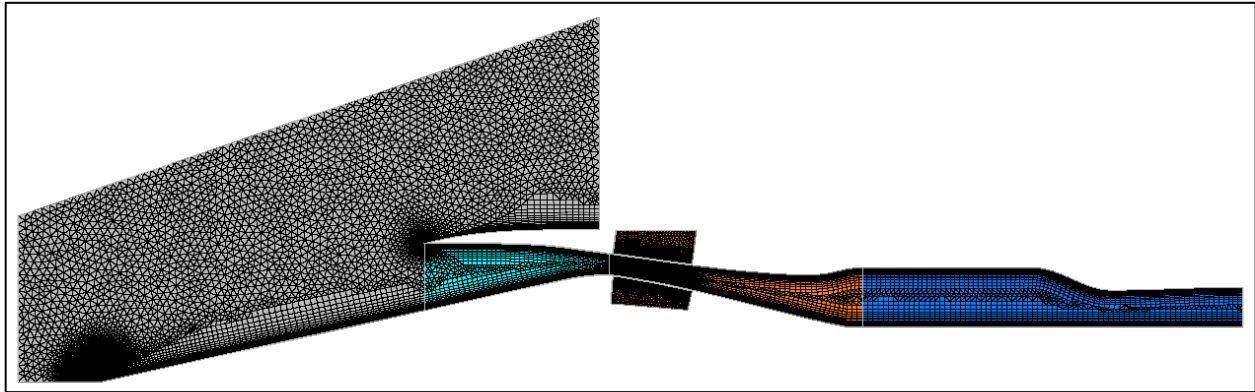
Figure 15 Four separate volume zones provide accessible integration interfaces.

Certain participants used custom grids instead of the ones provided by Cadence. Participants 2, 5 and 8 used two-dimensional and three-dimensional multi-block structured grids for Models A and B. The multi-block, structured grids featured a C-grid that wrapped about the cowl lip to provide resolution of the flow. Within the interior ducting of inlet in the axial direction from the cowl lip to the engine face the grid contained 1,061 grid points. The streamwise spacing between grid points in the bleed regions was 0.00176 ft. In bleed regions III and IV each of the bleed segments contained 13 streamwise grid points. Between the centerbody and cowl the grid contained 251 grid points. The grid spacing normal to the inlet surfaces was 1.0E-05 ft, which resulted in $y^+ < 1.0$ for the first grid point off the inlet surface for resolution of the boundary layer. Across grid block faces, the grid lines matched with grid lines of their adjacent blocks. The grid blocks for the outflow nozzle are included within the grid. Changes to the throat area of the outflow nozzle involved switching out these blocks for the grid with the new throat area. The planar grid was used for planar, axisymmetric CFD simulations. A three-dimensional grid was generated by extruding the planar grid about the axis-of-symmetry for the sector of 27 degrees. The grid contained 91 grid points in the circumferential direction and these grid points were evenly spaced about the circumference. A singular axis boundary condition was applied for the grid block boundary that collapses to the axis-of-symmetry upstream of the nose of the centerbody spike. Finally, participant 6 used the three-dimensional multi-block structured grid and modified it using a solution-adaptive approach for Model C. Participant 4 used a cartesian adaptive approach for all test cases in Models C and D, applied to the corresponding Cadence grids. Participant 5 also used a customized grid for Models C, D and E that was generated using METACOMP's grid generation tool MIME.

III. Grid Sensitivity Study

The different PAW grids for Models B, C and D are compared using the CFD results for Case 2 as most of the experimental data available for validation corresponds to that operating condition. Only submitted data by Participant 3 is used to assess the influence of the grid. A discussion of the computational results is presented for all the different flow metrics separated by inlet modelling approach (B, C or D) and by grid resolution level (coarse, medium, or fine). The conclusion of this comparison is that for this given flow solver and flow solver settings, the best prediction of the mixed-compression inlet performance is achieved with the finest possible grids and the most realistic inlet modelling approach, which is in-grid vortex generators and, if possible, in-grid bleed system.

No significant differences between grids or grid refinement level can be found just by observing the data at the provided boundary layer rakes. Only in the final centerbody and cowl interior rakes can it be noted that the more refined grids predict a sharper flow transition at the final viscous sublayers. This happens at around h = 0.22 in the centerbody rake and at h = 0.72 inches in the cowl interior rake (Figure 16). The influence of the grid refinement is less than the influence of the model, as it can be seen in the entries with the same color scheme collapsing on top of each other in Figure 16.
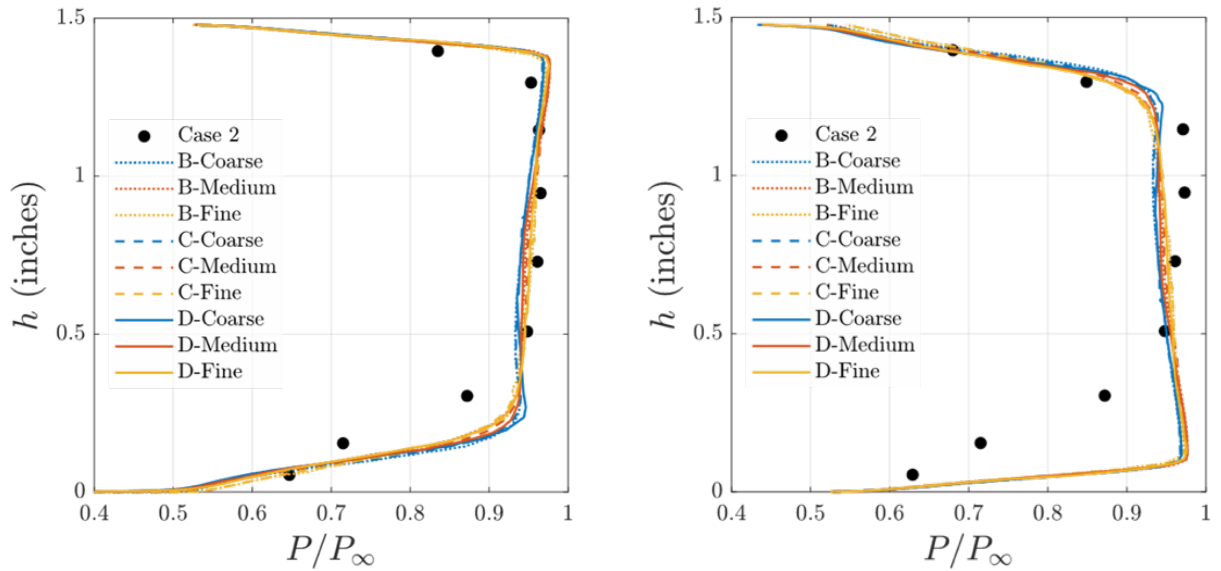

Figure 16 Centerbody (left) and cowl (right) throat rakes at x/Rc = 3.751.

In terms of the static pressure profiles across the centerbody and cowl interior, these indicate that models B and C capture sharper spikes at the limiting points of the bleed regions than model D (Figure 17). This may be linked to the abrupt change of flow properties at the edge of the surface bleed boundary condition at bleed zones III and IV. Upstream the bleed regions, there are no significant differences between models. However, downstream the main bleed regions (x/Rc ≈ 4 and onwards), models C and D show a delayed increase in static pressure in relation to the case 2 experimental data, bringing model D slightly closer to the experimental data compared to model C. This can be linked to the presence of the fully resolved vortex generators. Model B captures the static pressure field better in the vicinity of the bleeds and, in the cowl interior case, also at high x/Rc values. Models C and D, despite their delayed prediction of static pressure increase, show better performance at predicting the static pressure at high x/Rc values, with no significant differences between model C and model D. The grid refinement has a minor influence on the prediction than the geometry model in other regions except the bleed zones, where finer grids bring the CFD solution slightly closer to the experimental data, indicating that all provided solutions are not grid independent especially in the vicinity of the porous bleed areas.
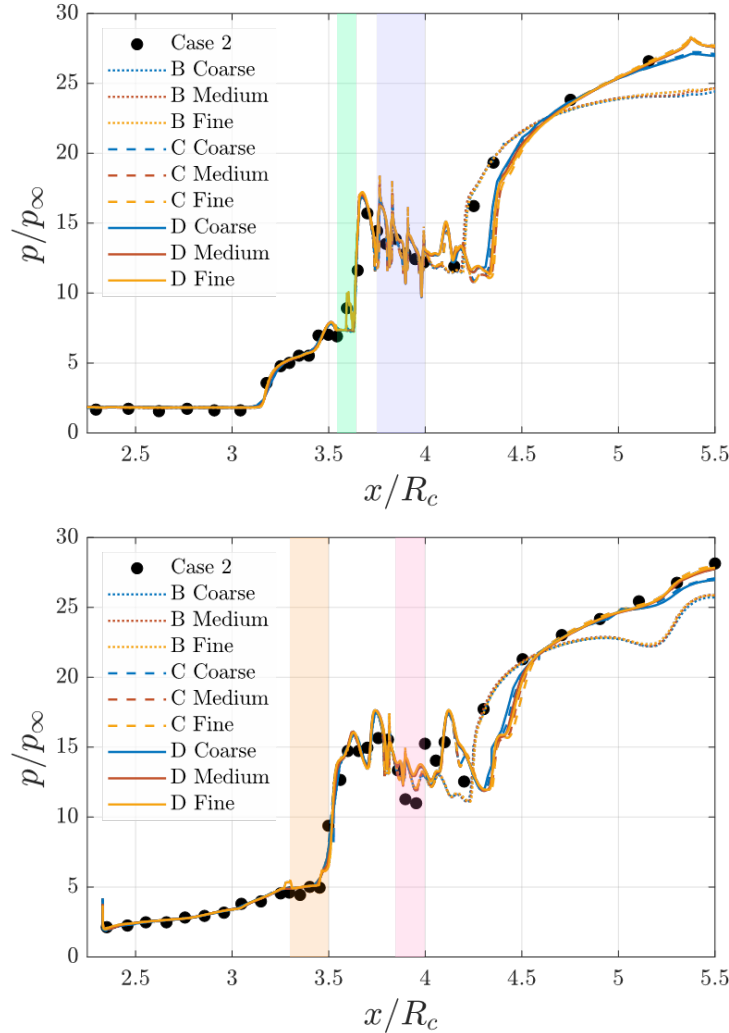
Figure 17 Centerbody (top) and cowl interior (bottom) static pressure profiles for Case 2 across the range of grids. Highlighted regions represent the location of the different bleed zones.

Finally, when it comes to the engine face total pressure recovery, results with models C and D are noticeably closer to the Case 2 experimental 2 than Model B results (Figure 18 left). This can be directly linked to the presence of the fully resolved vortex generators. Grid refinement influences the predictive capability of models C and D as finer grids seem to agree better with the wind-tunnel results. This is not the case with model B, where the grid refinement factor does not seem to have influence in the computational values. In terms of the overall inlet performance, cane data in Figure 18 right, show that all models significantly underpredict the pressure recovery for the Case 2 flow ratio, $\dot{m}_2/\dot{m}_\infty$, without great variations between the various model configurations. Models C and D overall appear closer to the experimental results, and do not have big differences between one another. Model B has a noticeably lower total pressure ratio than the other two models. In all cases, increasing the level of grid refinement has a slightly positive effect on the CFD prediction of the experimental data, especially from the point of view of the mass flow ratio.
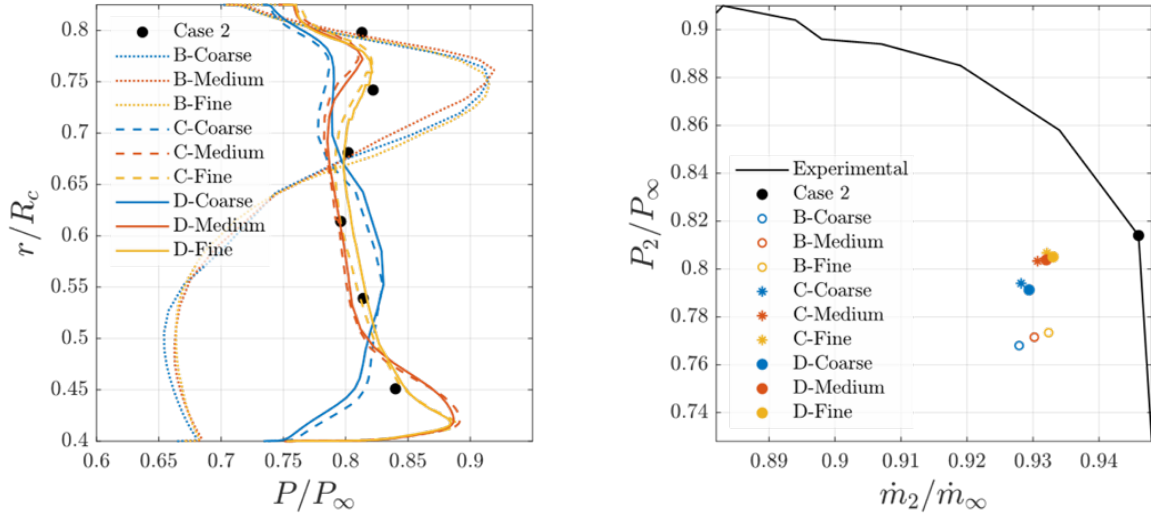
Figure 18 Average engine face total pressure recovery (left) and overall intake performance (right) for the various models and grids for Case 2 submitted by participant 3.

IV. Results and Discussion

In this section comparative plots including submitted results from all participants are shown for a given model configuration that was used to simulate the operating point indicated as Case 2 (Figure 6). Most participants provided data to enable comparisons against the available experimental data with regards to the incoming boundary layer characteristics, static pressure distributions along the cowl and the centerbody of the inlet as well as engine face total pressure recovery radial distributions and cane data. A common nomenclature system to distinguish between the different test cases submitted was constructed. A label identifier for each data entry in all the figures shown hereafter follows the structure described in Figure 19; participant number, preceded by inlet model in some cases where different models are plot together in the same figure, followed by grid type/refinement specification, turbulence model used, and optional approaches used by some participants, such as adjusted plenum pressures (p^*), reduced throat area at the plenum (t^-) or different axial stations during measurement (x^*). Most of the comparisons were conducted for Case 2 (Figure 6) which was the test case most participants simulated. A smaller number of submissions included Cases 8, 4 and 5 and these are discussed later in the section.

(M.) P. G. T. X

M – Model, A to E
P – Participant, 1 to 7
G – Grid label identifier
T – Turbulence model
X - Additional attributes

Figure 19 Nomenclature definitons used for submitted datasets identification.

A. Case 2 Model B results

Model B (Figure 8) was a simplified representation of the intake system with all porous bleed regions I to IV modelled as surfaces with sources. No notion of vortex generators was included. Flow predictions submitted by participants 3, 5, 7 and 8 are shown hereafter for the finest grid available for each participant. In most of the presented flow metrics, data from participant 3 showed the best agreement with the Case 2 experimental data. Overall, all flow metrics are well-predicted by the CFD results except for the engine face total pressures and the mass flow measured at the canes.

The flow solver and grid configuration had a major impact on the predicted results for Case 2 using Model B. This can be seen in Figure 20, where notable differences are observed between Participants 5 and 7 boundary layer characteristics in the approaching boundary layers at x/Rc = 2.771 and x/Rc = 3.250. Participant 7 submitted predictions made with several different turbulence models that, at some regions below the transition region of the boundary layers, show differences between single and multi-equation turbulence modelling approaches. The grid refinement factor plays a secondary role especially at locations where the incoming boundary layer was not fully developed, as it can be seen both with Participant 5 (two-dimensional and three-dimensional grids) and Participant 7 (medium and fine PAW grids) results (Figure 20 top Figure 21 left). No significant influence of grid or solver is seen at the last cowl or centerbody rake profiles at x/Rc = 3.751 where all CFD predictions seem to agree with each other (Figure 20 bottom Figure 21 right).
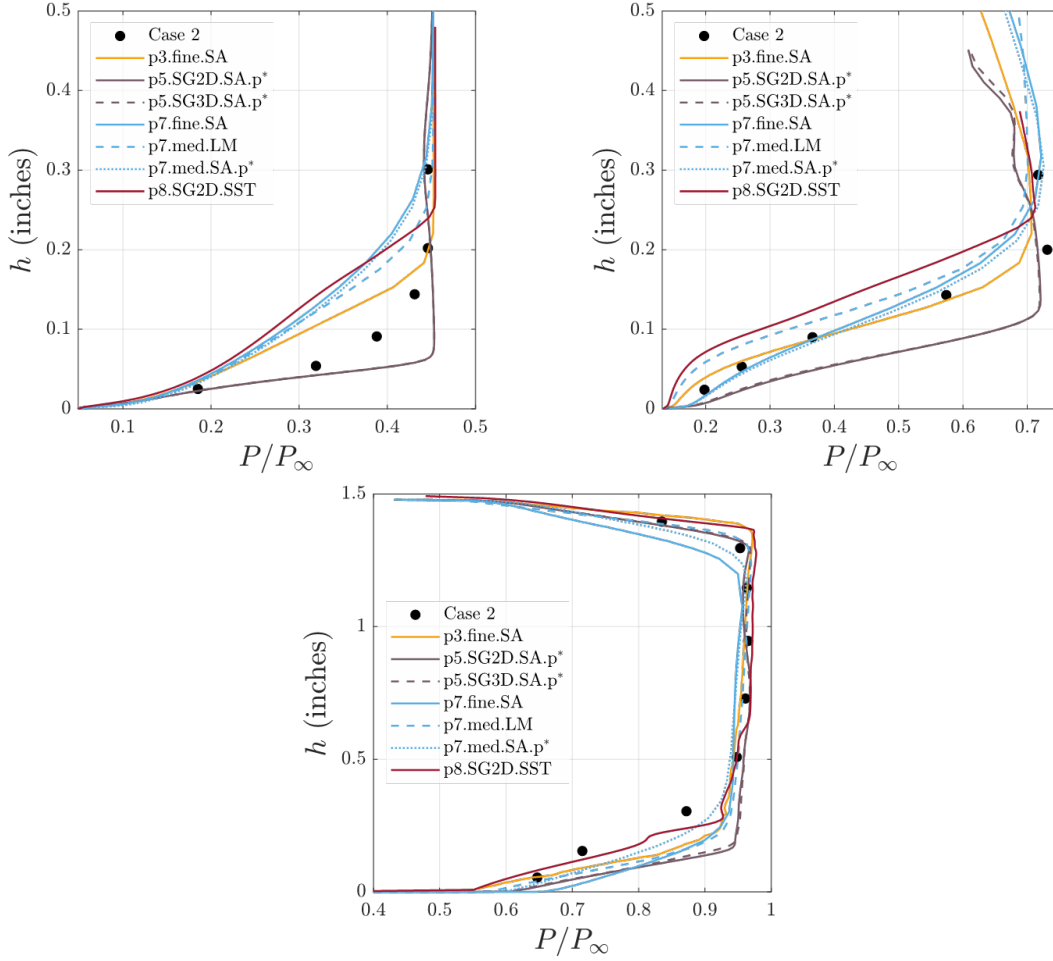
Figure 20 Centerbody Rake 1 (x/Rc = 2.771, top left), Rake 2 (x/Rc = 3.250, top right) and Rake 3 (x/Rc = 3.751, bottom) for Case 2 using Model B and various grid configurations.
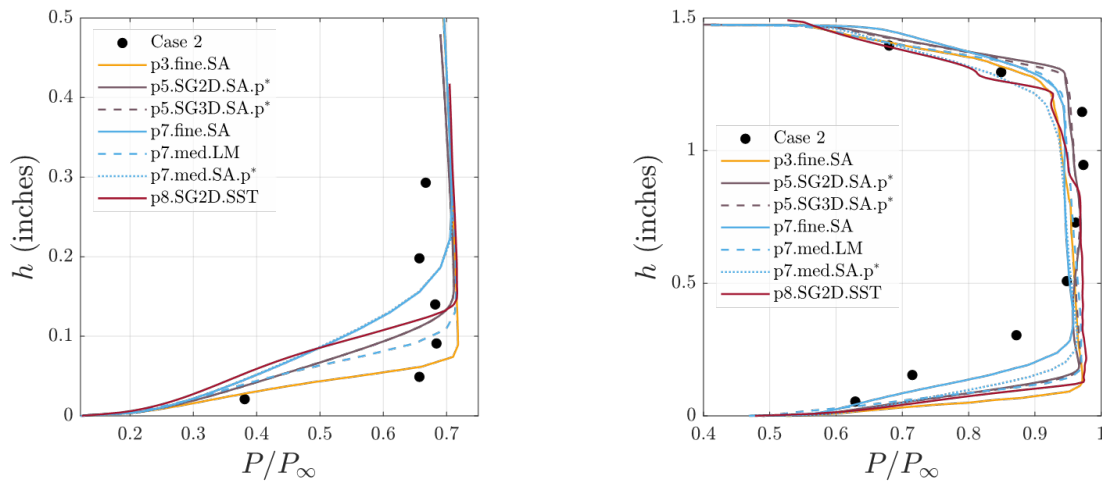

Figure 21 Cowl Interior Rake 1 (x/Rc = 3.250, left) and Rake 2 (x/Rc = 3.751, right) for Case 2 using Model B and various grid configurations.

Published by the American Institute of Aeronautics and Astronautics with permission.

In terms of pressure distributions over the cowl and centerbody, no significant differences were observed across all submitted CFD predictions which agreed well with the wind tunnel data for x/Rc < 3.15 (Figure 22). A slight discrepancy can be observed in Participant 8 cowl interior variation (Figure 22 bottom) which was conducted on a 2-dimensional grid that seems to predict a constant static pressure up to bleed region I at x/Rc = 3.15. Across the porous bleed regions between x/Rc = 3.5 and x/Rc = 4, the CFD predicted static pressure variations broadly follow the trend shown by the wind tunnel data. However, close comparisons cannot be safely made partially due to the sparsity of the test data and partially because the porous patches included in Model B are only represented by surfaces, rather than fully resolved bleed holes. As a result, the influence of the grid type, refinement level, flow model used or other modelling approaches such as turbulence model or adjusted bleed pressures cannot be safely assessed. Finally, in all cases, all CFD datasets underpredict the static pressure ratio for x/Rc > 4.25 both in the cowl and centerbody, which is possibly linked to the fact the bleed flows are overpredicted hence the flow downstream of the porous region is over-expanded (Figure 22).
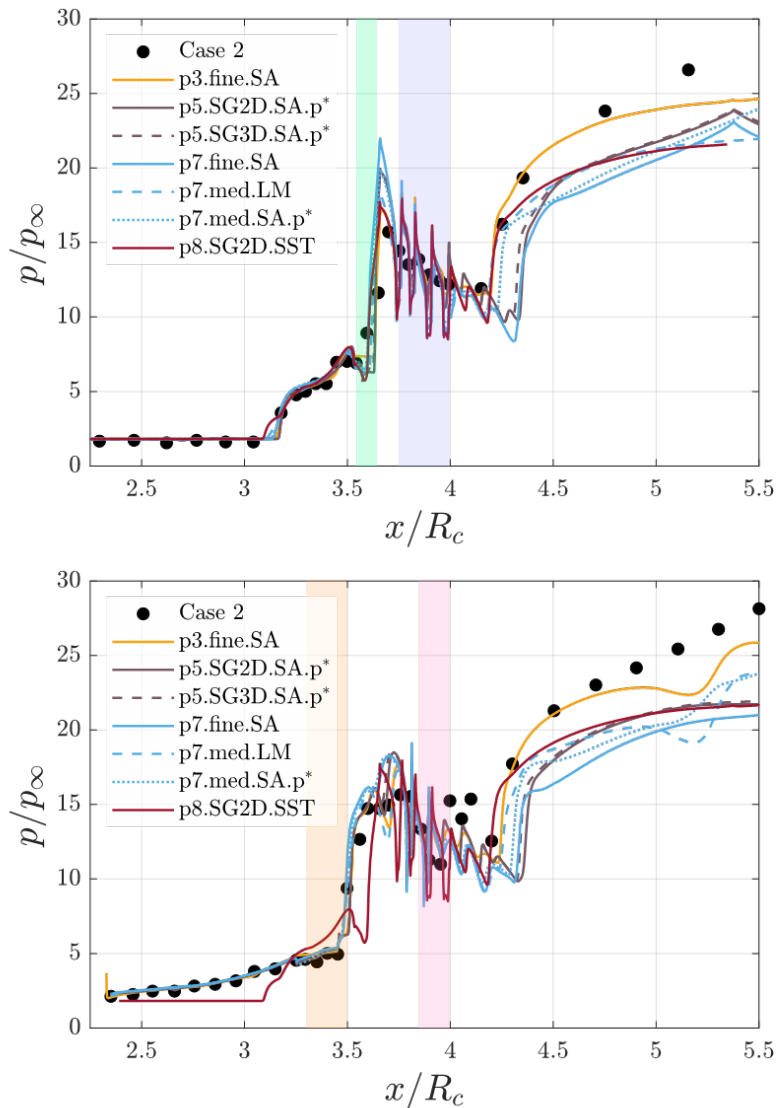
Figure 22 Centerbody (top) and cowl interior (bottom) static pressure profiles for Case 2 using Model B and various grid configurations. Highlighted regions represent the location of the different bleed zones.

Finally, looking at the engine face total pressure recovery profiles for the 27-degree sector modelled, Model B predictions show very poor agreement with the wind tunnel data with a maximum discrepancy of the order of 30% (Figure 23 left). This observation can be potentially linked to poor modelling of the flow separations along the subsonic diffuser downstream of the post-throat shock train. The poor engine face modelling is also reflected in the cane curve of Figure 23 right, where all CFD data sets indicate a notably lower flow ratio in relation to Case 2 test data for broadly the same measured pressure recovery. The flow solver used by each participant appears to be the most influential parameter.
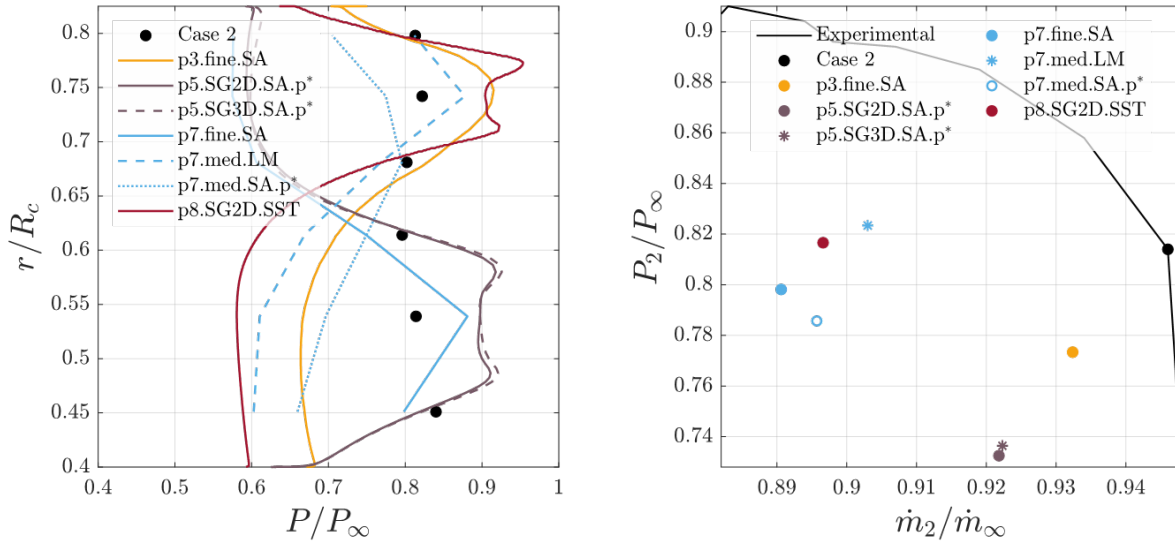
Figure 23 Engine face total pressure recovery (left) and cane curve (right) for Case 2 as predicted by Model B for various grid configurations.

B. Case 2 Model C results

Model C (Figure 9) also included the porous bleed areas as surfaces but in this case a set of vortex generators was part of the geometry which were fully resolved as airfoil profiles (Figure 4 and also see [5] for further details). All CFD submissions for this case were made on different computational grids; participant 4 used a grid adapted from the coarse PAW D grid which has many elements much smaller than the other participants. Participant 6 used a grid adapted from the fine PAW D grid using an adapted metric derived from the Mach residuals.

In general, all predicted boundary layer profiles at the inlet's centerbody were found in good agreement with the wind tunnel data (Figure 24). In terms of the cowl interior profiles, data from participant 3 show a shorter boundary layer height at the first measurement station with $x/Rc = 3.250$ (Figure 25 left). All CFD data sets seem to predict a notably different boundary layer profile at the second cowl station with $x/Rc = 3.751$ (Figure 25 right) which would yield significant variations in the shape factor at this is particular location. This is not the case at the last centerbody station with $x/Rc = 3.751$ where the predicted boundary layer profiles seem to be in better agreement with the test data. Participant 4 data shows small regions with reverse flow in the last centerbody and cowl interior stations in Figure 24 bottom and Figure 25 right, respectively. Overall, the radial flow profile, and hence the vorticity budget, introduced at the engine face is notably different between the test data and all CFD predictions which may justify discrepancies in the radial total pressure recovery coefficients.
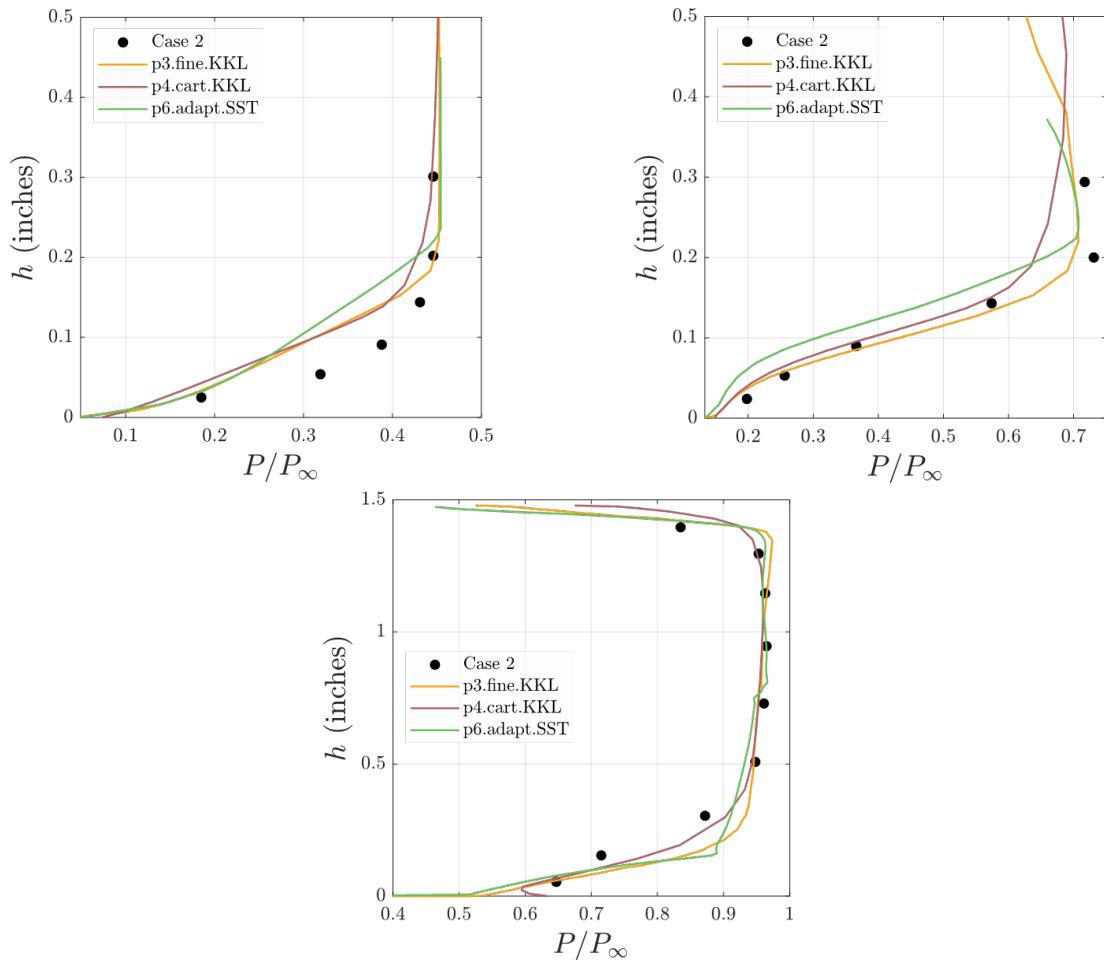
Figure 24 Centerbody Rake 1 (x/Rc = 2.771, top left), Rake 2 (x/Rc = 3.250, top right) and Rake 3 (x/Rc = 3.751, bottom) for Case 2 using Model C and various grid configurations.
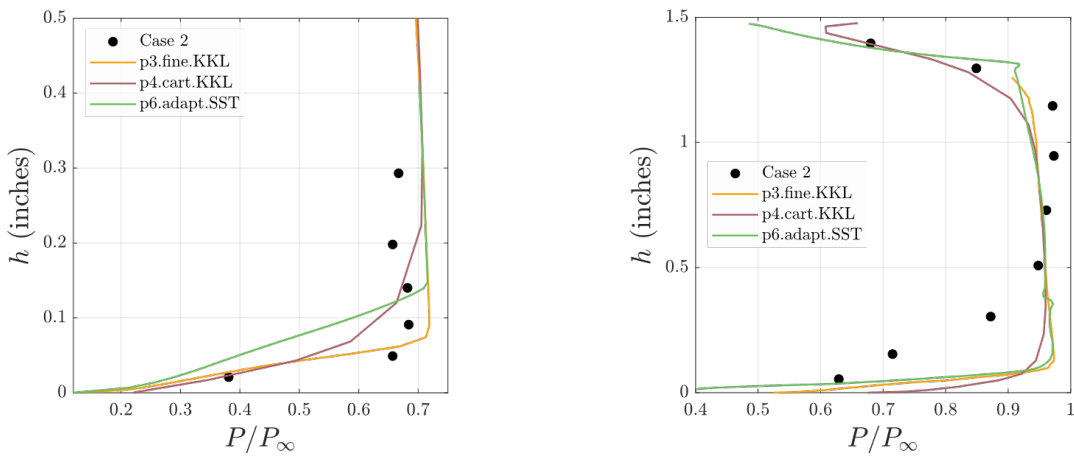

Figure 25 Cowl Interior Rake 1 (x/Rc = 3.250, left) and Rake 2 (x/Rc = 3.751, right) for Case 2 using Model C and various grid configurations.

When it comes to the static pressure distributions along the cowl interior and centerbody, a similar set of observations to the previous case when Model B was use can be made here with regards to the predictions upstream and along the porous patch regions (x/Rc < 4.5), which broadly agree with the wind tunnel data across the range of participants (Figure 26). Again, it remains difficult to extract solid conclusions about the predictions along the porous regions as Model C had also no notion of fully resolved holes. For the section downstream of the porous patches, where the vortex generators are located (x/Rc > 4.5), there notably good agreement can be observed between the predicted and measured data, which was not the case with Model B previously (Figure 22). This is attributed to the existence of the vortex generators whose potential field seems to be dominant in this part of the domain and well predicted both in its near- as well as in its far-field as the vortex generators are fully represented in Model C.
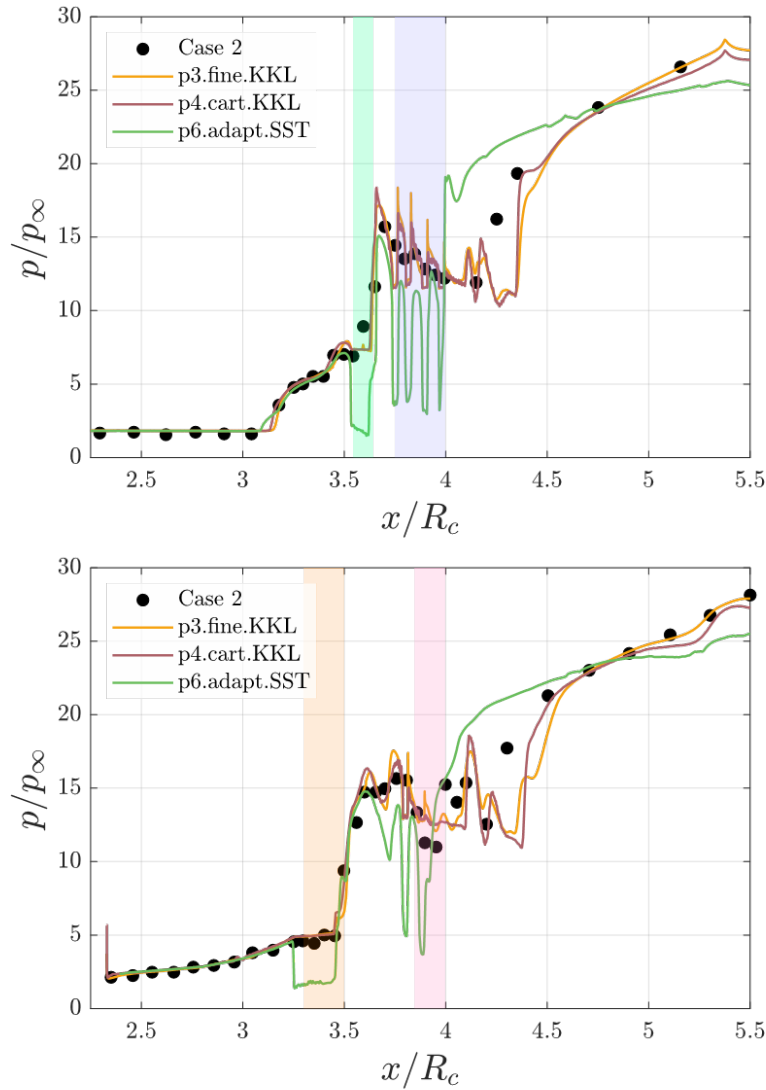
Figure 26 Centerbody (top) and cowl interior (bottom) static pressure profiles for Case 2 using Model C and various grid configurations. Highlighted regions represent the location of the different bleed zones.

Finally, looking at the engine face total pressure radial profiles, the submitted data from Participants 3 and 4 show very good agreement with the Case 2 experimental data (Figure 27 left). Participant 6 results overpredict the total pressure ratio at the bulk of the flow indicating that the wakes coming off the vortex generators have not been completely mixed up with the rest of the rest of the flow. In terms of the overall intake performance as reflected on the cane curve (Figure 27 right), a maximum discrepancy of two percentage units in flow ratio is noticeable in Participant's 6 dataset which comes with a significant underprediction of the engine face total pressure recovery. The other two datasets from Participants 3 and 4 show a one percentage unit discrepancy in flow ratio with relation to the test point and very good agreement in terms of engine face pressure recovery.
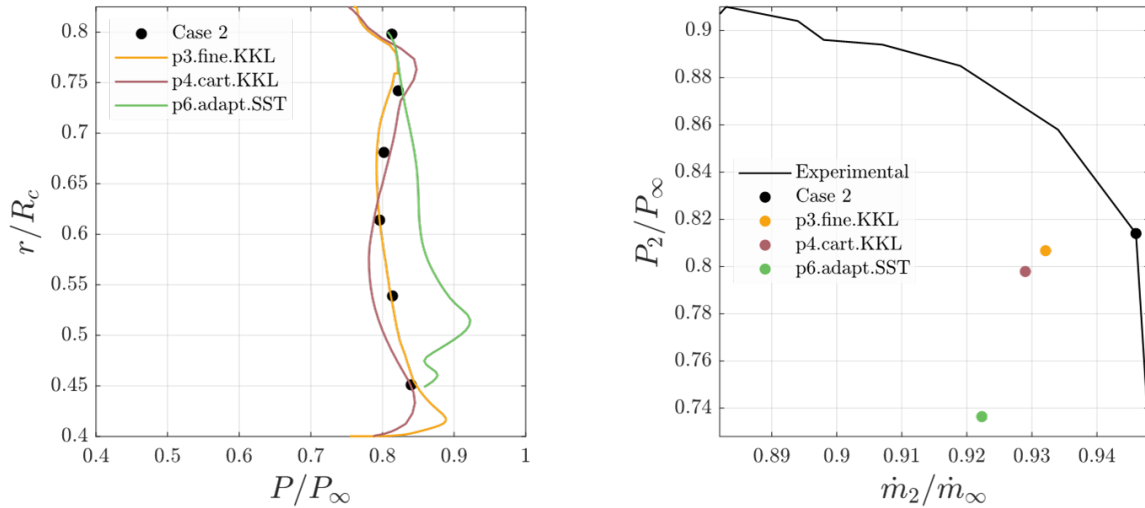
Figure 27 Engine face total pressure recovery (left) and cane curve (right) for Case 2 using Model C and various grid configurations.

C. Case 2 Model D results

A large number of cases was submitted by participants who used Model D for their simulations. Model D (Figure 10) features bleed zones I and II as surfaces, while bleed zones III and IV were fully resolved with discrete holes and plenums. In addition, all vortex generators are fully resolved and meshed as airfoil profiles as in Model C. Multiple participants submitted files for this case/model combination, using a wide range of numerical settings. Most participants used the PAW grids, while Participant 4 used an adapted grid with a very low element count compared to its counterparts. Participant 5 used both a fine PAW grid and an in-house grid created in the grid generation tool MIME.

From the comparisons between the submitted CFD results against the Case 2 wind tunnel data it is observed that no CFD result fully agrees with the measured data, especially for the two first locations with x/Rc = 2.771 and x/Rc = 3.250 (Figure 28 top left and right, Figure 29 left). Generally better agreement is observed at the last rake location with x/Rc = 3.751. Data sets from Participants 1 and 5 show the closest fit to the Case 2 data in most viscous zones of the boundary layers. In most cases, data from Participant 7 show notably thicker boundary layers across all measurement locations both at the cowl as well as at centerbody.
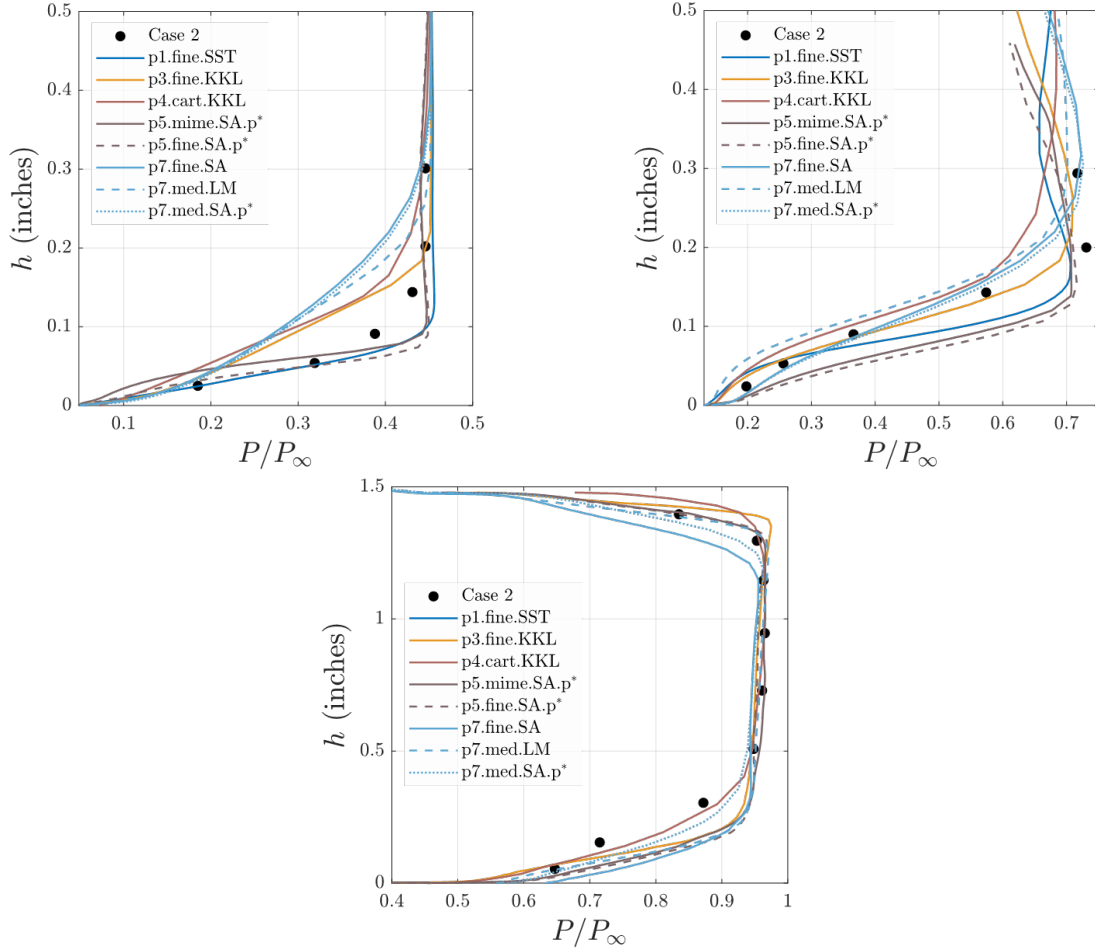
Figure 28 Centerbody Rake 1 (x/Rc = 2.771, top left), Rake 2 (x/Rc = 3.250, top right) and Rake 3 (x/Rc = 3.751, bottom) for Case 2 using Model D with various grid configurations.
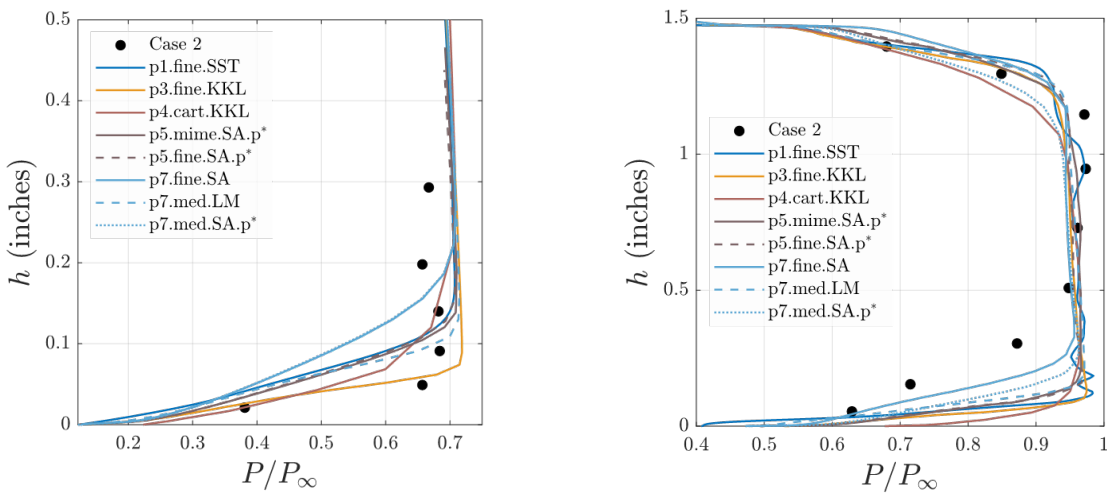

Figure 29 Cowl Interior Rake 1 (x/Rc = 3.250, left) and Rake 2 (x/Rc = 3.751, right) for Case 2 using Model D with various grid configurations.

In terms of static pressure distributions, as in previous configurations with Models B and C all predictions agree remarkably well with the wind tunnel data upstream of the bleed region II and across bleed region I for x/Rc < 3 (Figure 30), while post-bleed (x/Rc > 4.25) static pressure variations are generally underpredicted except for Participants 3 and 4 datasets where a fine PAW grid was used for the simulations. Along the bleed region, as previously, although all CFD models follow the trend showed by the test data, it is probably hard to draw conclusions due to the low resolution of the experimental information in this part. However, data sets by Participant 7 show that (Figure 30 top) even across the bleed region, the CFD prediction is very little affected by the grid size or the turbulence closure (light blue lines in Figure 30).
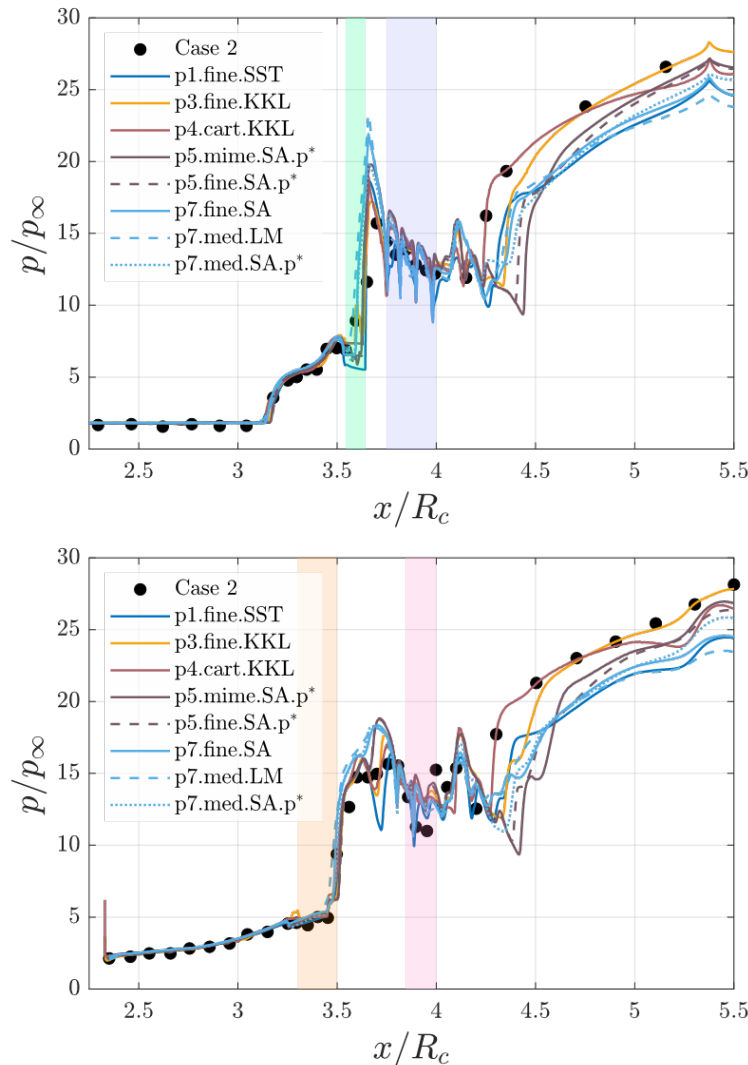

Figure 30 Centerbody (top) and cowl interior (bottom) static pressure profiles for Case 2 using Model D with various grid configurations. Highlighted regions represent the location of the different bleed zones.

Finally, in terms of engine face pressure recovery radial profiles, Participants 3 and 4, with the PAW fine grid for Model D, show the best agreement with the test data (Figure 31 left), while submissions by Participant 7 show a notable under prediction of the spanwise pressure recovery across the range of grids and turbulence models used for these simulations. In terms of overall inlet performance, all submitted datasets show poor agreement with the Case 2 engine face overall pressure recovery, while the flow ratio measured at Case 2 is also notably underpredicted (Figure 31 right).
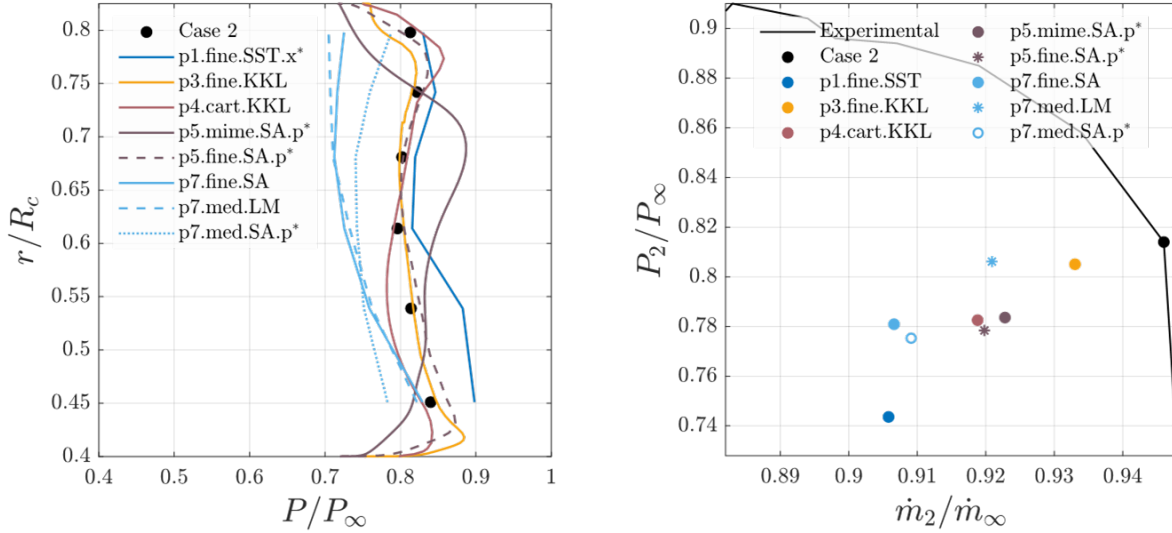
24

Figure 31 Engine face total pressure recovery (left) and cane curve (right) for Case 2 using Model D with various grid configurations.

D. Case 2 Models A and E results

The last family of submitted results used Models A and E for a limited number of simulations (a total of 4 cases was submitted). In both Model A (Figure 7) and E (Figure 11) configurations the vortex generators were modelled as source terms (using the BAY model [9]). In terms of bleed region modelling in Model A all porous regions are represented by surfaces with uniform flow applied onto them, whereas in Model E bleed regions I and II are represented by surfaces, while bleed regions III and IV are fully resolved with meshed, discrete holes as well as underpinning plenum chambers. None of the submitted solutions with Models A or E relied on any of the PAW issued grids. Simulations with Model A were conducted using two- and three-dimensional grids [6] [7]. Simulations with Model E were conducted with a customised grid by Participant 5 that was developed using the MIME tool. Most of the CFD results submitted here use a modified bleed pressure, compared to what was provided in [5], to drive the bleed flows and facilitate full convergence at the bleed regions.

In all four cases, the centerbody boundary layer profiles were found to be about 30% thinner than what the test data suggest across all three measurement locations (Figure 32). This is also the case at the cowl interior locations (Figure 33), suggesting that total pressure profiles at engine face might be influenced as distortion is highly dependent on incoming flow profiles. Participant 5 data with the modified MIME grid on Model E indicate a slightly higher boundary layer at the centerbody compared to the other submissions (Figure 32), which approximates better the Case 2 test data especially at the transition between bulk flow and boundary layer region.
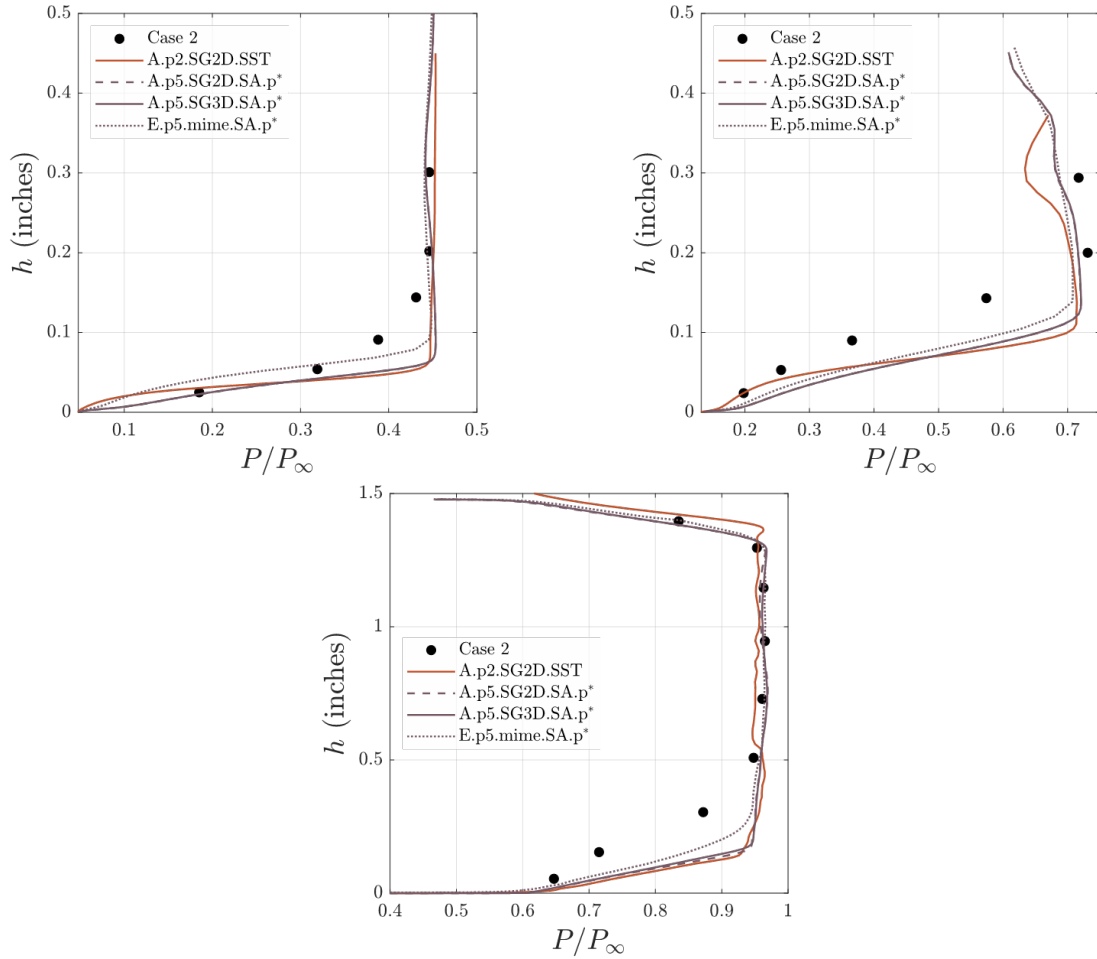
Figure 32 Centerbody Rake 1 (x/Rc = 2.771, top left), Rake 2 (x/Rc = 3.250, top right) and Rake 3 (x/Rc = 3.751, bottom) for Case 2 using Models A and E with various grid configurations.
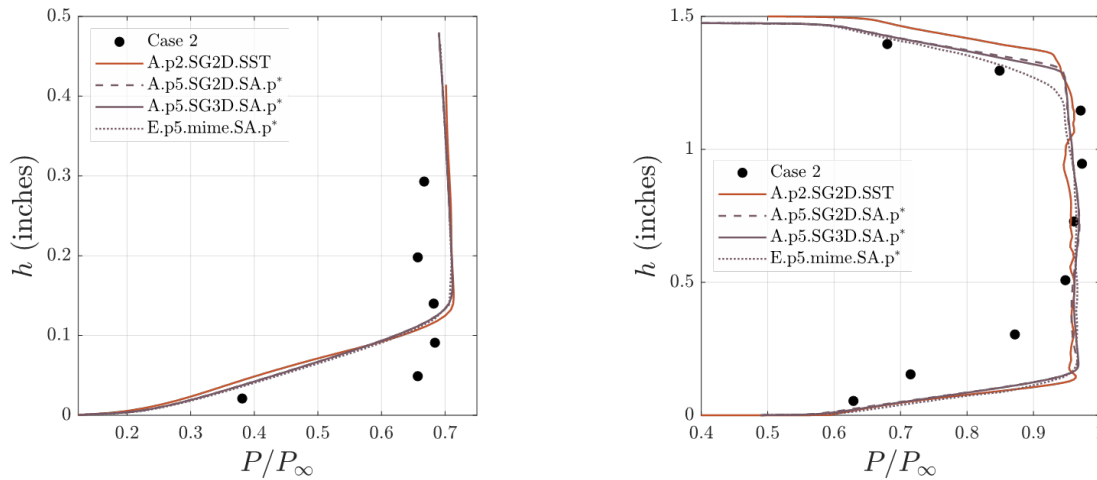

Figure 33 Cowl Interior Rake 1 (x/Rc = 3.250, left) and Rake 2 (x/Rc = 3.751, right) for Case 2 using Models A and E with various grid configurations.

In terms of static pressure distributions, similar observations apply on this case as in all previous ones. Pressure profiles upstream of the bleed area are all well calculated, while the pressure variations across the bleed patches are also broadly captured (Figure 34). Again, due to the low spatial resolution of the test data it is hard to extract and safe conclusions in relation to the predicted pressure variations across this part. Looking at the post-bleed pressure variations the two-dimensional grid by Participant 2 indicates a close agreement with the Case 2 test data in both centerbody and cowl interior surfaces. The other models broadly follow the test data trend but generally at about 10% lower levels of non-dimensional pressure.
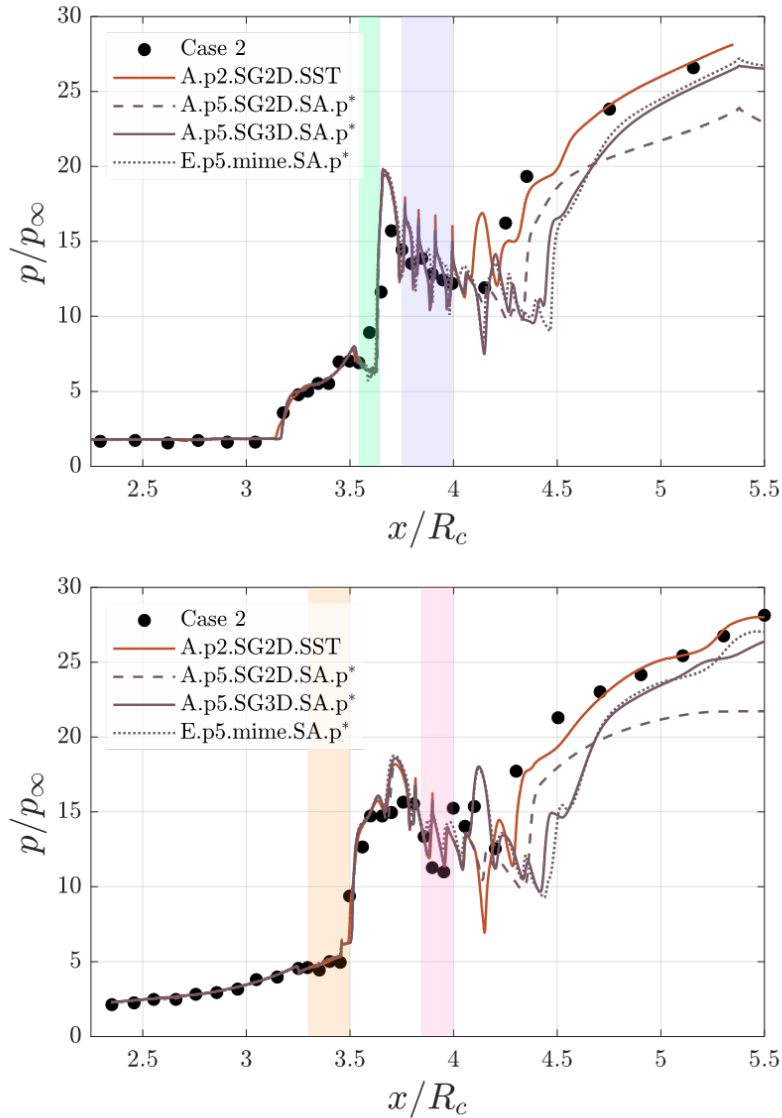

Figure 34 Centerbody (top) and cowl interior (bottom) static pressure profiles for Case 2 using Models A and E with various grid configurations. Highlighted regions represent the location of the different bleed zones.

As in all previous cases where Models B, C or D were used, noticeable disagreement between the various submitted datasets and the experimental data can be seen at the Model A/E engine face total pressure recovery profiles (Figure 35 left). Model E results with the MIME grid was found able to accurately capture the radial variation of the pressure profile at engine face, suggesting that the influence of the inlet boundary layer profile on the total pressure distortion is significant (Figure 32 top left). However, in all four submitted cases there is a two-percentage point under prediction

of the flow ratio (Figure 35 right), probably influenced by the variation in the total bleed flow extracted upstream. Pressure recovery is also slightly under predicted, even by Model E results, except in the two-dimensional case which seems able to predict the Case 2 test value of approximately 0.82. This observation is suggesting that three-dimensional flow effects across the 27-degree sector seem to be affecting the time averaged flow distribution across the plane especially in these cases where the vortex generator system is not fully resolved as part of the grid but only modelled via source terms.
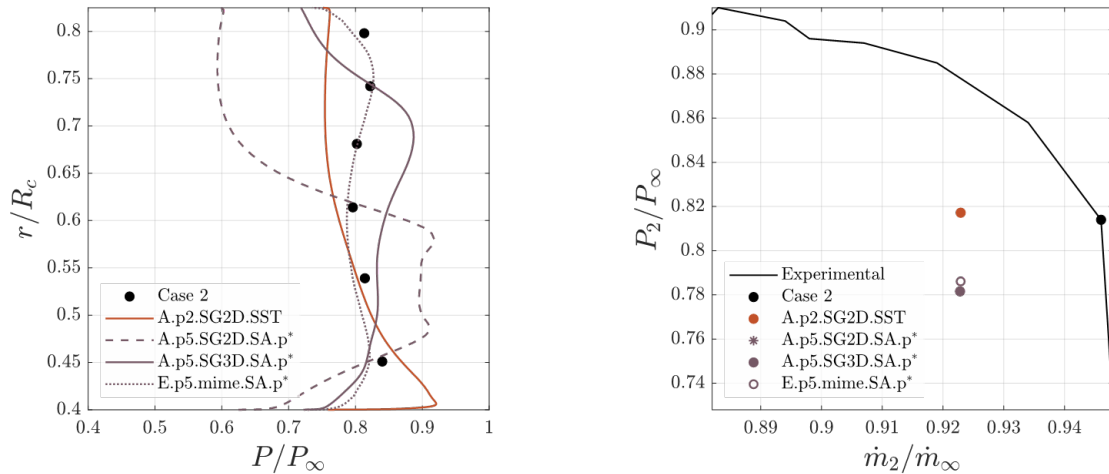

Figure 35 Engine face total pressure recovery (left) and cane curve (right) for Case 2 using Models A and E with various grid configurations.

E. Case 8 results

Case 8 was an optional test case at a sub critical operating point provided to the PAW participants (full description in Figure 6). A number of CFD simulation data sets was submitted by various participants using mainly Models B, C and D (Figure 8, Figure 9 and Figure 10) which allows for some comparisons to be made. For Case 8 only the static pressure profiles along the centerbody and cowl, as well as engine face total pressure profiles and cane data were made available.

All submitted numerical data sets were able to produce good predictions outside the throat and stability bleed regions, with x/Rc < 3.65 or x/Rc > 4 (Figure 36). Across the inlet regions at the vicinity of the throat, at x/Rc between 3.6 and 4, models B and C slightly underpredict the experimental pressure ratio while model D overpredicts this, perhaps linked to the bleed system modelling approach. Models B and C show similar results within the bleed regions, and in Model D participant 3 predicts higher pressure spikes than Model 4. Participant 8 used a reduced throat area at the plenums to enhance convergence at the bleed regions and a different turbulence modelling approach than the other entries, but this does not seem to have a considerable influence in the selected flow metrics.
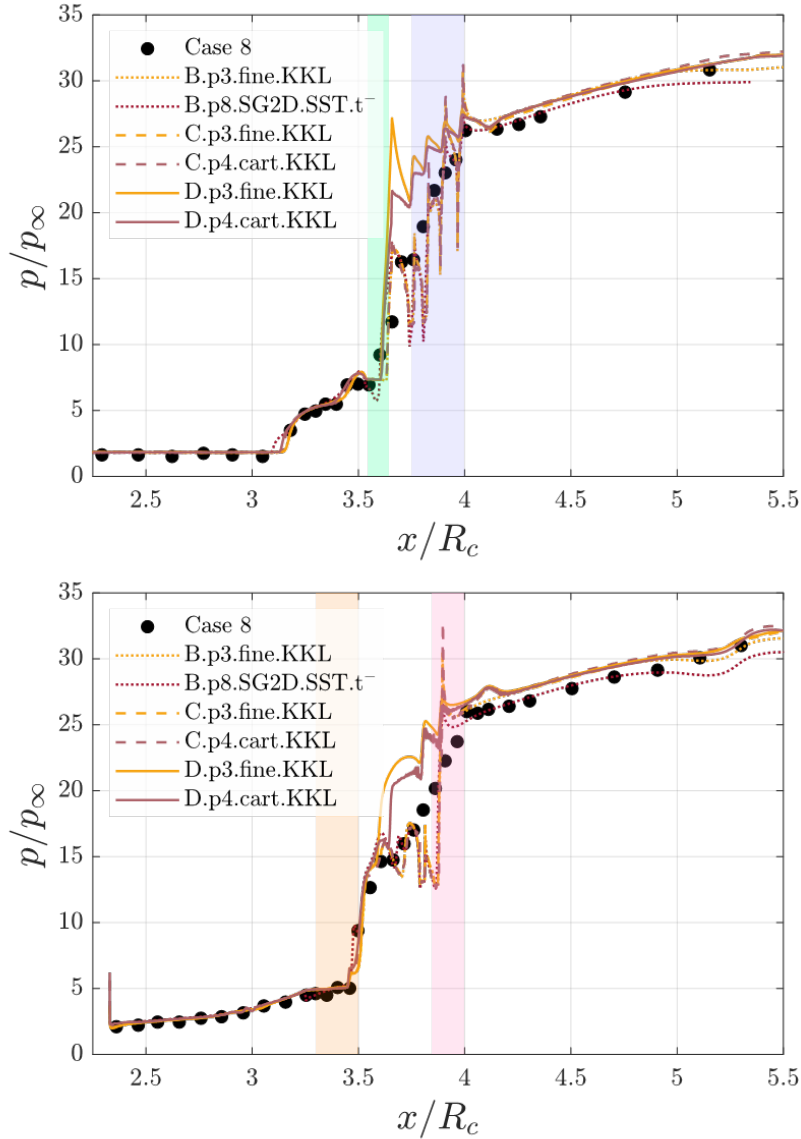
Figure 36 Centerbody (top) and cowl interior (bottom) static pressure profiles for Case 8 using Models B, C and D with various grid configurations. Highlighted regions represent the location of the different bleed zones.

In terms of engine face total pressure recovery profiles, most models indicate a fair prediction of the radial variations (Figure 37 left), but models C and D are superior in accuracy compared to the experimental data, probably because of the vortex generator flow physics. Model D slightly excels at predicting the Case 8 validation data, likely due to a better bleed system modelling accuracy. Results with Model B relied on a different grid configuration, turbulence model, flow solver and plenum modelling approaches, so it is not possible to establish the cause of the differences between Participant 3 and 8 results. Finally, cane curve data indicate a general poor ability to predict Case 8 flow ratio across all model and numerical setups. The total pressure ratio is, overall, well-predicted by all participants and models (Figure 37 right).
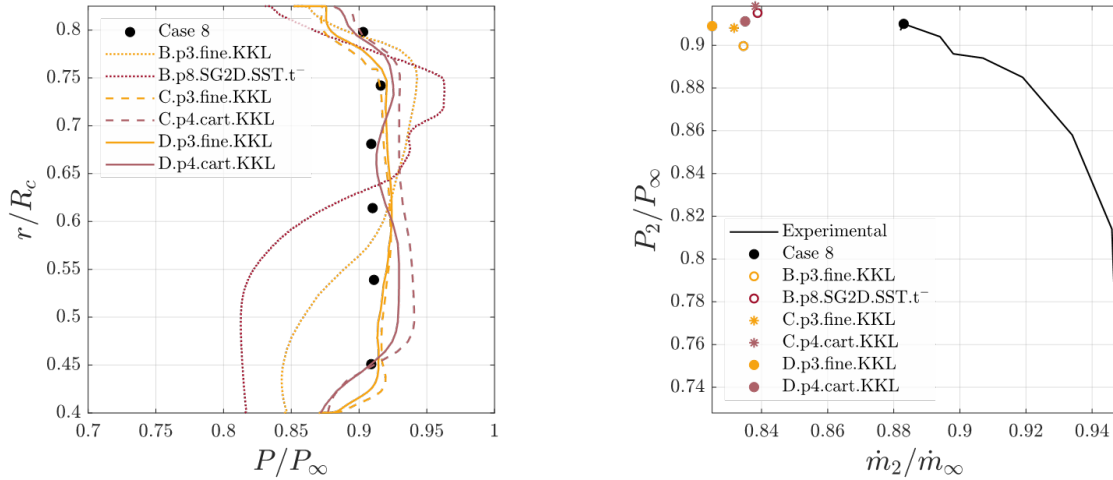
Figure 37 Engine face total pressure recovery (left) and cane curve (right) for Case 8 using Models B, C and D with various grid configurations.

F. Case 4 and 5 results

Cases 4 and 5 were also provided as an optional case with a flow ratio of 0.919 for Case 4, that is between Cases 2 and 8 flow ratios (Figure 6). For this case, submissions using Models A, B, C and D were also made either with the fine PAW grid or with custom grids. For Case 5, all models and flow solvers offer a good prediction of the static pressure ratio profiles along the inner cowl and centerbody (Figure 38). In the bleed regions highlighted in Figure 38, model D shows a slight over prediction of the static pressure ratio than models B and C, which predict very similar results between one another. This may be due to the presence of an in-grid bleed system in model D, whereas models B and C have a modelled bleed.
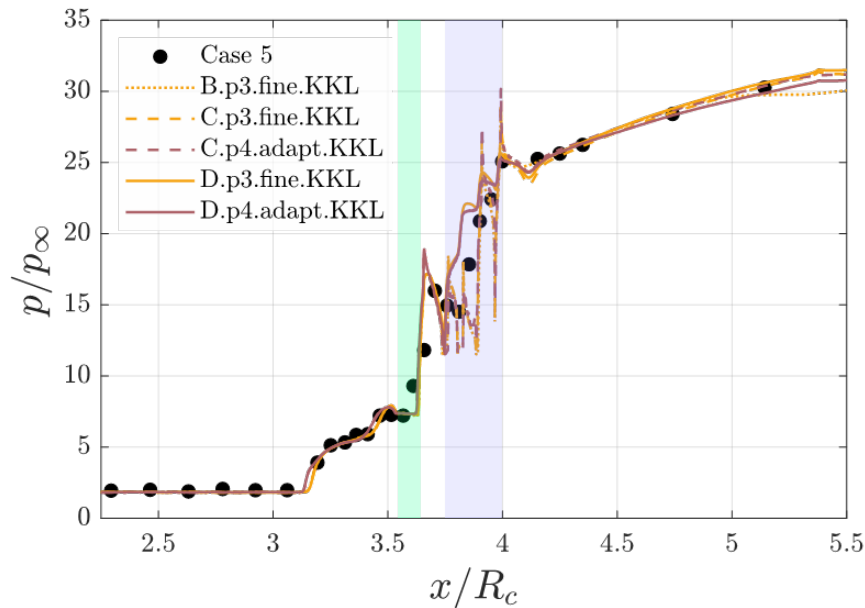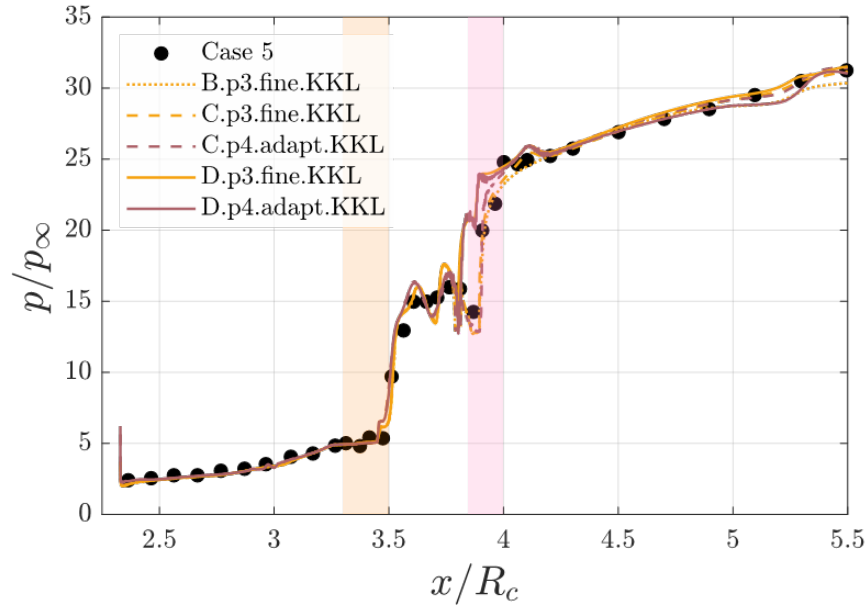
Figure 38 Centerbody (top) and cowl interior (bottom) static pressure profiles for Case 5 using Models B, C and D with various grid configurations. Highlighted regions represent the location of the different bleed zones.

For Case 4, engine face total pressure radial profiles were only submitted by Participants 2 and 8 on a two-dimensional grid. Both datasets are shown in Figure 39 left in comparison with the available rake data for this case. The comparison shows that none of the two models was able to follow the test data trend, but it is very hard to link this to a specific modelling characteristic. Participant 2, with a simple BAY model for vortex generators, produced a slightly better prediction of the Case 4 data than participant 8, where no notion of vortex generators was included either modelled or meshed. In terms of cane data, as in Case 8, there is a notable flow ratio under prediction across all models, but the total pressure ratio agrees with the experimental results (Figure 39 right).
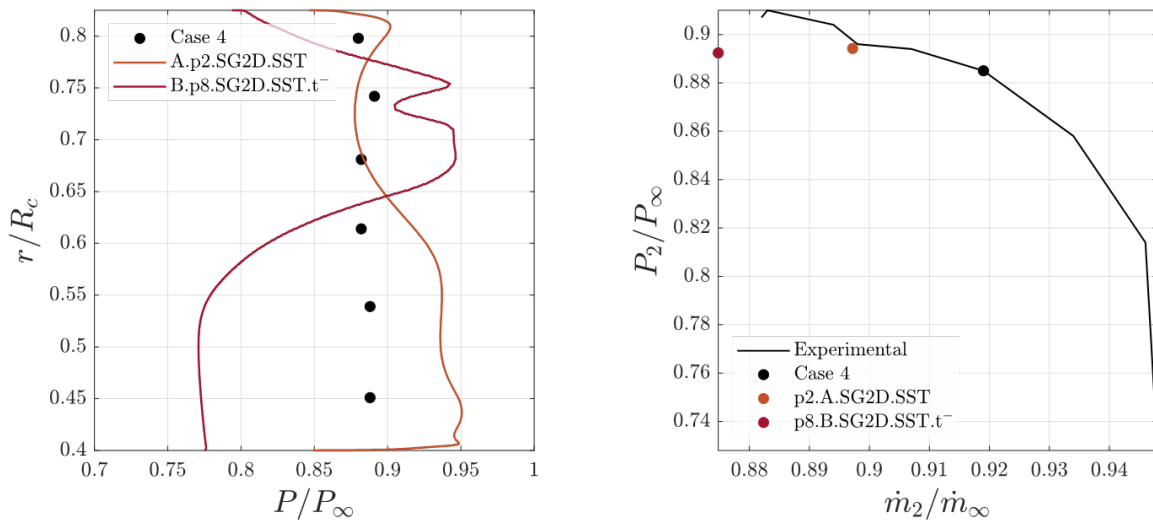

Figure 39 Engine face total pressure recovery (left) and cane curve (right) for Case 4 using Models A, B, C and D with various grid configurations.

V. Summary and Conclusions

Accurate predictions of the complex flow through a mixed compression inlet with bleeds and vortex generators remains very challenging for the CFD community. The NASA 1507 inlet test was investigated as part of AIAA's 6th Propulsion Aerodynamics Workshop, and the findings are summarized in this paper. Although an overwhelming number of numerical results was submitted by many participants, the comparisons against the historic wind tunnel data produced inconclusive outcomes about the ability of modern CFD tools to predict the flow characteristics across the various operating points. This is partially due to the complex aerodynamics that characterize the internal shock system of the mixed compression inlet, where porous bleeds work in conjunction with the vortex generator system and partially due to the nature of the available test data, which in many cases lack the required spatial resolution to allow understanding of the underpinning flow mechanisms. However, from the presented studies the following conclusions were extracted:

- **Case 2 boundary layers**: low variability between inlet modelling approaches and grid refinement levels for all rakes was found, except at the last centerbody and cowl interior rake where higher grid refinement levels improve the predictions, indicating that no grid convergence was achieved with the provided grids in terms of incoming boundary layers.
- **Case 2 static pressures profiles**: broadly all participant results predicted well the distribution along the centerbody and cowl interior upstream of the porous bleed regions. Downstream of the bleeds, most models underpredict the static pressure profiles. Models C and D are generally slightly better. Along the porous areas models capture the axial bleed locations, but the participants using an in-grid approach for the discrete bleed holes and plenums produced a smoother pressure distribution than the cases where modelled bleed flows were used. The latter typically featured higher magnitude spikes. In general, models D and E show better agreement to the wind tunnel across all bleed zones.
- **Case 2 engine face rake**: Model B shows poor predictions regardless of the numerical setup of grid used. Models C and D, in general, show better agreement than model B, possibly due to the presence of fully resolved vortex generators. Fully resolved bleed systems, on average, improve the predictive capability of the average engine face pressure data as well. However, a solid conclusion is hard to be made, as the only clear comparison features very few participant entries with very different flow solver configurations.
- **Case 2 cane data**: all participants and models underpredicted the flow ratio. In general, inlet model, flow solver setup and grid refinement level were all found to play a key role in the modelling of the system performance.

For Cases 4, 5 and 8, it is also hard to establish any conclusive remarks to characterize the validity of the flow predictions, as the submitted results were very different in terms of flow solver setup and grids. In general:

- **Static pressures**: as in Case 2, along the porous bleed zones, model D overpredicts the bleed static pressure data while models B and C show closer agreement to the experimental data across all submitted case. It is hypothesized that the modelling fidelity of the porous bleed plays a key role as the bleed mass flow rates were not fully compared between the various test cases but clearly influence the prediction.
- **Engine face rake**: as in Case 2, model B provides a poor prediction of the experimental data, while the other inlet models show slightly better agreement, likely linked to the presence of vortex generators.
- **Cane data**: all entries underpredict the mass ratio proportionally to the inverse of the bleed total pressure ratio. In general, Case 8 shows less accurate predictions than Cases 4 or, on average, Case 2. As in the previous cases, it is hard to draw any conclusion rather than, for every flow solver, finer grids and fully resolved bleed system models with the underlying plenums, were found better able to predict the available experimental data.

Acknowledgments

References

[1] Chyu, W. J., Kawamura, T. and Bencze, D. P., "Calculation of External-Internal Flow Fields for Mixed-Compression Inlets," NASA TM X-88362.

[2] Abedi, M., Askari, R., Younsi, J. S., and Soltani, M. R., "Axisymmetric and three-dimensional flow simulation of a mixed compression supersonic air inlet," *Propulsion and Power Research*, 2020; 9(1), pp. 55-61.

[3] Baydar, E., Lu, F. K., Slater, J. W., and Trefny, J. C., "Vortex Generators in a Streamline-Traced, External-Compression Supersonic Inlet," 55th AIAA Aerospace Sciences Meeting, 9-13 January 2017, Grapevine, Texas.

[4] Sorensen, N. E., and Smeltzer, D. B., "Investigation of a Large-Scale Mixed-Compression Axisymmetric Inlet Capable of High Performance at Mach Numbers 0.6 to 3.0," Publication NASA TM X-1507, February 1968.

[5] 6th AIAA Propulsion Aerodynamics Workshop Inlet Test Case Guide, available at https://paw.larc.nasa.gov/paw-6-inlet-test-case/

[6] Slater, J. W., and Saunders, J. D., "Modeling of Fixed-Exit Porous Bleed Systems for Supersonic Inlets," *Journal of Propulsion and Power*, Vol. 26, No. 2, 2012, pp. 193–202. https://doi.org/10.2514/1.37390

[7] Slater, J., "Improvements in Modeling 90-Degree Bleed Holes for Supersonic Inlets," *Journal of Propulsion and Power*, Vol. 28, No. 4, 2013, pp. 773–781. https://doi.org/10.2514/1.b34333

[8] Frink, N. et al., "A Boundary Condition for Simulation of Flow Over Porous Surfaces," 19th Applied Aerodynamics Conference, June 11-14, 2001.

[9] Dudek, J. C., "Modeling Vortex Generators in a Navier–Stokes Code," *AIAA Journal*, Vol. 49 No. 4 pp. 748-759, April 2011.

2024-01-04

Summary of the 6th Propulsion Aerodynamics Workshop: NASA 1507 Inlet

Moreno, Miguel

AIAA